Low-dimensional perovskite materials and their optoelectronics

Tao Zhu and Xiong Gong*

School of Polymer Science and Polymer Engineering, College of Engineering and Polymer

Science, The University of Akron, Akron, OH 44325, USA

Abstract

Three-dimensional (3D) organic-inorganic metal halide perovskite materials possess great potential applications for approaching efficient optoelectronics due to the unique optoelectronic properties of perovskite materials and cost-effective manufacturing possibilities of optoelectronics. But, the scientific and technical challenges of 3D perovskite materials were their inferior long-term stability, which hampered their practical applications. The low-dimensional perovskite materials composed of alternating organic and inorganic layers are one of the most credible paths toward stable perovskite photovoltaics and optoelectronics. In this short review, we first present a discussion of the crystal structure and nontrivial optoelectronic properties of the low-dimensional halide perovskites. The synthetic methods for the preparation of the low-dimensional halide perovskites are reviewed. After that, we focus on the recent development of perovskite photovoltaics, light-emitting diodes, and lasers by the low-dimensional halide perovskites. Finally, we outline the challenges of the low-dimensional halide perovskites and their applications.

*Corresponding author, Email: xgong@uakron.edu; Fax: (330) 9723406

Content

1. Introduction

Three-dimensional (3D) halide perovskites have shown outstanding optoelectronic properties, such as strong light-harvesting capability, high light absorption coefficient (~10^5 cm^{-1}), low trap densities, high photoluminescence quantum yield (PLQY), narrow-band emission, and low exciton binding energies (<50 meV).[1-8] These unique features enable 3D perovskite materials to have great potential applications in solar cells,[9-12] photodetectors (PDs),[13-16] light-emitting diodes (LEDs),[17-20,] and lasers.[21-22]

The growth of photovoltaics by 3D perovskites was unprecedented in the past decade.[23-26] So far, over 25.2% power conversion efficiencies (PCEs) from perovskite solar cells (PSCs) by 3D perovskites with a small device area (< 1 cm^2) have been demonstrated and photodetectivities of ~10^{15} Jones (1 Jones = 1 cm Hz$^{1/2}$W^{-1}) have been reported from perovskite PDs (PPDs) by 3D perovskites.[25, 27] Moreover, a PLQY of over 90%, which was an ultra-high value, was reported from 3D perovskite quantum dots.[28] The laser exhibited ultralow-threshold (220 nJ cm^{-2}) and high-quality factors (Q≈3600) at a charge carrier density of $1.5×10^{16}$ cm^{-3} from 3D perovskite single-crystal were also demonstrated.[29] However, the instability of 3D perovskite materials against moisture, light, and heat was still a key challenge, which hindered practical applications of 3D perovskite materials in photovoltaics and other optoelectronics.[30-32] Many efforts have been devoted to enhancing the stability of 3D perovskite materials over the past several years. These approaches included interfacial modification,[33-34] additives processing,[35] lowering dimensions,[36] tolerance factor adjustment[37,] and encapsulation techniques.[38] Among them, the concept of utilization of 3D perovskites embedded with low-dimensional perovskites has been demonstrated to be a promising approach for suppressing degradation of perovskite materials.[39-43]

The most commonly studied low-dimensional perovskites were Ruddlesden-Popper (RP)-phase 2D perovskites (**Scheme 1a**), which was composed of alternating organic and inorganic layers with a general formula, $A_2A'_{n-1}B_nX_{3n+1}$, in which A is the longer organic cation (e.g., $C_8H_9NH_3^+$ or PEA^+), A' is the shorter organic cation (e.g., $CH_3NH_3^+$ or MA^+), B is the metal cation (e.g., Pb^{2+} or Sn^{2+}) and X is the halide anion (e.g., I^- or Cl^-), n is the numbers of metal halide layer between organic spacers and organic layers.[44] Alternatively, organic cations with two amino groups on both ends thereby removing the van der Waals gap between the layers (**Scheme 1b**), which could form a more stable Dion-Jacobson (DJ)-phase 2D perovskites with a general formula, $AA'_{n-1}B_nX_{3n+1}$. For alternating cations in the interlayer space (ACI) phase 2D perovskite with a formula, $A_2A'_nB_nX_{3n+1}$, the shorter organic cation (MA^+) fills in both corner-sharing $[BX_6]$ metal halide network and interlayer (**Scheme 1c).**

Different from shorter organic cations (e.g., $CH_3NH_3^+$ (MA^+)) in 3D perovskite materials, longer organic cations (e.g., $C_8H_9NH_3^+$ (PEA^+)) with hydrophobic properties in 2D perovskite materials could slow down the degradation process in (2) step described below:[45]

$$PbI_2 + MAI \Longleftrightarrow MAPbI_3 \quad (1)$$

$$MAPbI_3 + H_2O \Longleftrightarrow MAPbI_3 \cdot H_2O \quad (2)$$

$$(4-n)MAPbI_3 + nMAPbI_3 \cdot H_2O + (2-n)H_2O \Longleftrightarrow (MA)_4PbI_6 \cdot 2H_2O + 3PbI_2 \quad (3)$$

$$(MA)_4PbI_6 \cdot 2H_2O \Longleftrightarrow PbI_2 + 4MAI + 2H_2O \quad (4)$$
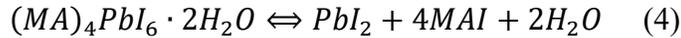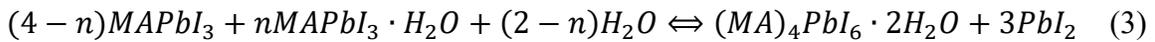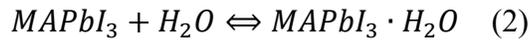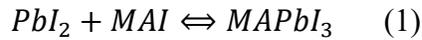
In addition, the electrically insulating nature of a long organic spacer and perovskite conductor layers could lead to the natural multiple-quantum-well structures, as shown in **Schemes 2a & 2b**.

The organic spacer layers serve as the potential "wall" and the perovskite layers serve as the potential "well". In this case, the excitons are formed in the low-dimensional perovskite

materials instead of free charge carriers due to increased binding energy induced by quantum confinement and the generated electroluminescence in the low bandgap regions, which was confined effectively by higher energy gap regions, resulting in an efficient radiative charge carrier recombination.[46-47] These unique properties could make the low-dimensional perovskite materials to be great candidates for LEDs and laser applications.[48-49] As the organic layer thickness is increased, the quantum confinement effects are prominent, consequently resulting in blue-shifted absorption and emission.[39] The large bandgap of pure two-dimensional (2D) perovskite materials (n=1) certainly renders themselves less desirable for solar cell applications. Therefore, the low-dimensional perovskites with a larger n (n>3) are proposed to be candidate materials for approaching efficient PSCs and PPDs.

In this short review, we firstly give a discussion of the crystal structures and optoelectronic properties of the low-dimensional perovskites. Secondly, the synthetic methods for the preparation of the low-dimensional halide perovskites are summarized. After that, the overview of the applications of solar cells, PDs, LEDs, and lasers are discussed. Finally, a summary and key challenges toward high-performance optoelectronic applications of the low-dimensional perovskites are outlined.

2. Crystal structure and nontrivial optoelectronic properties

2.1 Multiple quantum well structures in 2D perovskites

The low-dimensional perovskite materials are composed of a corner-sharing $[BX_6]$ metal halide network sandwiched between the organic barrier planes of A.[50-51] The variable n is the stacking number of the $[BX_6]$ network layers between two organic barrier layers. In the case of n=1, the thickness of the $[BX_6]$ network layers decreases to the scale of de Broglie wavelength,

leading to a strong quantum confinement effect on the charge carrier's behaviors.[46] As a result, the charge carriers transport in 2D perovskites with n=1 is expected to be highly confined within the multiple quanta well (MQWs) structures. It is prevailingly agreed that the electrons under this condition are freely movable along the in-plane direction but are restricted in the out-of-plane direction. Theoretically, 2D perovskites with n=1 are ideal materials for LEDs application as it has natural the out-of-plane self-termination and is expected to exhibit 100% PLQY. Unfortunately, recent studies indicated that a low quantum yield observed from the low-dimensional perovskites suggested that the quantum losses was taken place within these materials.[40] So far, this is still an open question because of the lack of fundamental knowledge, such as exciton reduced mass and the spatial extension of the charge carriers wavefunctions.[52]

Various macroscopic techniques have been applied for the investigation of the MQWs structures of 2D perovskites.[53-55] Mohite and his colleagues demonstrated the importance of the Coulombic interactions in the low-dimensional perovskites.[54] They proposed a generic formulation of the scaling of the exciton binding energy with the thickness of the [BX$_6$] layer, which is described by:

$$E_{b,1s} = \frac{E_0}{\left(1+\frac{n-3}{2}\right)^2} \qquad (5)$$

where $n=3-\gamma e^{-\frac{L_W}{2a_0}}$, a_0 (4.6 nm) is the Bohr radius of 3D perovskites and the exciton ground state binding energy, E_0 (16 meV) is 3D Rydberg energy, L_W is the physical width of quantum wells (QWs) for an infinite QW potential barrier (i.e. 0.641 for (BA)$_2$Pb$_1$I$_4$, 1.255 for (BA)$_2$(MA)Pb$_2$I$_7$, where BA is butylammonium). In their model, the exciton is considered isotropic in an n-dimensional space (1<n<3) and the γ is an empirical correction factor (i.e. 1.76) for the deviations from the pure quantum confinement regime. The factor γ contains the electron and hole densities and dielectric confinement effects. Based on this model, the decrease in the value

of n would lead to a compression of the exciton wavefunction in the QW due to the dielectric confinement, which results in enhanced exciton binding energy. In the case of large n values, they further predicted that the exciton binding energy in the low-dimensional perovskites is higher than the thermal fluctuation ($k_BT=25.7$ meV) at room temperature as n values are larger than 20 ([BX_6] layers of ~12.6 nm). Certainly, this work provided a fundamental step towards the design of novel low-dimensional perovskite materials for optoelectronic applications, such as solar cells, PDs, LEDs, and lasers.

2.2 Edge states in 2D perovskites

In addition to considering the bulk physics in the low-dimensional perovskite materials, the layer edge states (ES) with nontrivial conducting phenomena in the low-dimensional perovskites have also been studied.[56] The ES in organic MQWs have untrivial properties. Fu et al. indicated that the ES states in HgTe QWs enable the dissipationless 1D electrical conduction.[57] Blancon and his colleagues reported that the free charge carriers at the ES within 2D perovskite [$(C_4H_9NH_3)_2(CH_3NH_3)_{n-1}PbI_{3n+1}$] can accelerate the exciton dissociation, which is favorable for solar cells application.[58] Recently, Priya et al.,[59] provided the direct observations of the distinct conductive layer ES in the low-dimensional perovskite single crystals ($C_4H_9NH_3)_2PbI_4$ (n=1) by conducting atomic force microscopy (c-AFM) mapping techniques. It was found that the out-of-plane current in the low-dimensional perovskite materials would behave as an insulating feature due to MQWs, and the out-of-plane current in the bulk terrace region was low, but an unexpected current along the contour of the layer edges was observed. Moreover, the current in the bulk terrace region was negligible but it became sharp at the layer edges. The huge difference between the bulk and the layer edge indicated that there were a number of free charge carriers presented at the ES layer and the bulk terrace region behavior as an insulating characteristic due to the

insulating organic layers. The total collected mobile charges per area across the layer edges are calculated by:

$$F = \frac{4}{3}\frac{E}{1-v^2}\sqrt{R}\delta^{\frac{3}{2}} \qquad (6)$$

$$\int I \cdot dy = \int \frac{dQ}{dt} \cdot dy = \int u \cdot dQ = u \cdot \int dQ \qquad (7)$$

where F is the force applied by the tip, E is Young's modulus, v is the Posson's ratio of the samples, δ is nanoindentation from the contact geometry, R is the radius of tip curvature, I is the detected current, dQ is the differential of free charge carriers and u is the local scan rate, respectively. Thus, the contact area determined by the nanoindentation δ and the total free charge carriers is estimated from Eq. (7). The charge carrier density at the ES was calculated to be $1.1 \times 10^{21} cm^{-3}$, which is close to that of metals ($10^{21} cm^{-3}$). Noted that the conducting nature at the layer edges would not change with the scan rates. For the insulating behavior of the bulk terrace region in the low-dimensional perovskite single crystals ($C_4H_9NH_3$)$_2$PbI$_4$ (n=1), the electrons and holes are heavily bonded with a binding energy of ~ 470 meV, leading to the formation of the exciton or further recombined through either photogeneration or injection from the electrodes. Such an investigation on the ES layer of the low-dimensional perovskite materials offers great opportunities for designing novel photovoltaic materials and their applications.

2.3 Crystal structure and bandgap in 2D perovskites

The crystal growth in the low-dimensional halide perovskite materials was also a significant difference compared to 3D halide perovskite materials. The latter one generally possesses multiple crystal planes, including the <100>, <110>, and <111> planes.[11] However, in the case of pure 2D perovskite materials (n=1), there are only the <100> groups that favor the continuous growth, giving rise to a poor charge carrier transport in the vertical direction.[60] As n is increased to over 1, the <110> and <111> planes start to grow, which are favorable for charge carrier

transport in the vertical direction since the oriented crystallization is parallel to the substrates, assisting in the growth of the charge-transport channels.

Compared to 3D perovskite materials, the low-dimensional halide perovskite materials show significantly different optical properties, which are dependent on dimensionality and size.[61] The bandgap (E_g) of a semiconductor refers to the minimum energy required for an electron to be excited from the ground state in the valence band (VB) to the conduction band (CB). Owing to the quantum confinement effect, the E_g of the low-dimensional halide perovskites can be varied by the values of n (the thickness of [BX_6]). For example, increasing the number of [PbI_6] layer affords a narrowing of the E_g from 2.24 eV for n=1 to 1.60 eV for n=4, in the case of $BA_2MA_{n-1}Pb_nI_{3n+1}$ perovskite.[62]

2.4 Influence of organic spacers on 2D perovskites

The long-chain organic spacers, as the crucial constituent, are essential to the optical and electronic properties of 2D perovskites. The commonly used organic spacer cations are listed in **Scheme 3.**

It was reported that the methyl groups anchoring on the ammonium N atom have a significant influence on the device performance of PSCs by 2D perovskites.[63] For example, Li et al.[63] reported 2D perovskites based on phenylammonium (PA, primary ammonium), N-phenylmethylammonium (PMA, secondary ammonium), N ,N -dimethylphenylammounium (DPA, tertiary ammonium), and phenyltrimethylammonium (PTA, quaternary ammonium) as organic spacers, and then fabricated PSCs by these 2D perovskites. They found that PSCs by 2D perovskites based on PTA organic spacer with three methyl groups exhibited the highest PCEs, which was possibly due to the altered rigidity, size, and dielectric constant of the organic interlayer spacer.[63]

In addition, it was found that the larger and more hydrophobic cations were beneficial for improving perovskite stability against moisture, although larger cations can adversely influence the device performance.[64] It was further found that the organic cations with flexible aliphatic hydrocarbons exhibited a better stereochemical configuration than rigid aromatic hydrocarbons.[65]

Studies have also demonstrated that controlling the QW width distribution was crucial to overcoming the performance-stability compromise in devices by 2D perovskites.[66] Sargent et al.[66] investigated how the organic spacer influences QW width distribution. They investigated 2D perovskites based on allylammonium (ALA) (Organic spacer (OS) 16), PEA (OS 4), and BA (OS 17) organic cations and found that ALA^+ could induce the formation of higher-n with monodisperse QWs in 2D perovskite film, which was ascribed to its single C=C bond could promote the intermolecular interactions between QWs. However, PEA^+ and BA^+ have higher formation energies due to the van der Waals and π-stacking interactions between cations, favoring the initial formation of low-n and polydisperse distribution QWs. Noted that polydisperse distribution QWs in 2D perovskites may act as ultrafast shallow traps for holes in materials, resulting in stronger recombination.[66]

3. Synthetic methods for the preparation of the low-dimensional halide perovskites

The first observation of quantum-confined 2D perovskite materials was reported by Tyagi et al.[67] They obtained a single-layer thick crystalline 2D methylammonium lead bromide ($MAPbBr_3$) perovskite by colloidal synthesis, where the octylammonium bromide was used as the long-chain ligand. The synthetic procedures involved adding lead bromide, methylammonium bromide, and octylammonium bromide into a stirring solution of oleic acid and 1-octadecene at 80 °C. The final 2D perovskite nanocrystals were obtained by further

dilution, filtration, precipitation, and re-dispersion. The nanostructures with various morphologies of perovskites can be obtained by controlling the purification of 2D MAPbBr$_3$ nanocrystals. The as-synthesized 2D MAPbBr$_3$ exhibited an obvious blue-shifted (~ 0.5 eV) absorption compared to 3D bulk MAPbBr$_3$, which is owing to the quantum confinements.[67]

3.1 Solution phase method

Yuan et al.[68] reported a one-pot synthetic method to prepare low-dimensional perovskite micro-disks, $(R_1NH_3)_2[(R_2NH_3)_2PbBr_4]_{(n-1)}PbBr_4$, where R_1 is a long octyl chain, R_2 is an aromatic alkyl group. The synthesis details are shown in **Scheme 4**. Hydrobromic acid was added into a dimethylformamide (DMF) solution containing aromatic methylamine (benzylamine or thiophenemethylamine), octylamine, and lead bromide to generate a yellow pale precursor solution, which was then injected into vigorous hexane and then stirred for 5 minutes (min) at room temperature, followed by acetone quenching. These 2D perovskites were only a few micrometers in lateral size with a thickness of 100-150 nm. They found that the as-synthesized perovskites exhibited significantly improved photophysical properties over 3D bulk perovskites, such as narrow deep blue emissions peaked at 403-413 nm, high PLQY of 53%, and good stability.

Dou and his colleagues further reported a direct growth of atomically thin 2D hybrid perovskite [(C$_4$H$_9$NH$_3$)$_2$PbBr$_4$] from the solution.[69] In detail, a very dilute precursor solution (C$_4$NH$_9$NH$_3$Br+PbBr$_2$+DMF) was dropped on the precleaned surface of Si/SiO$_2$ substrate and dried under 75 °C. After that, CB was selected as a co-solvent to reduce the solubility of (C$_4$H$_9$NH$_3$)$_2$PbBr$_4$ in DMF, promoting crystallization. It was found that the crystallization process was uniform across the whole substrate due to the similar boiling point and evaporation rate of DMF and CB. This method overcame the limitations of the conventional exfoliation and

chemical vapor deposition methods, which generally produced a thick perovskite plate. They found that the photoluminescence of the as-synthesized 2D perovskites was changed with the structural relaxation or the lattice-constant expansion. Aharon *et al*. presented a facile low-temperature synthesis of 2D perovskite nanorods (NRs).[70] The 2D NRs showed a shift to higher energies in the absorption and photoluminescence compared to 3D bulk perovskite. The formation mechanism of 2D NRs was analyzed by varying different ligands (from octylammonium to oleic acid). They further found that the bandgaps can be tuned from 1.90 eV to 2.26 eV by adjusting the halide from iodide to bromide.

Vybornyi et al. reported another synthetic method for the preparation of low-dimensional $CH_3NH_3PbX_3$, which was without polar solvents (DMF).[71] The reaction between methylamine and PbX_2 was conducted in a nonpolar solvent such as 1-octadeecne ODE at an elevated temperature in the presence of oleylamine (OLM) and oleic acid (OLA) as ligands in the precursor solution. The tetrahydrofuran (THF) solution containing methylamine and OLA was injected into the above precursor solution under vigorous stirring. The nanocrystals could be formed within seconds. They found that the low-dimensional perovskite nanocrystals exhibited either blue-emitting or green luminescent by adjusting the amount of OLM. The platelets with n=3 (approximately value) exhibited an absorption peaked at 450 nm and PL emission at 465 nm with a PLQY of 18%.

3.2 Vapor-assisted method

The low-dimensional perovskite materials prepared by vapor-assisted methods generally have better crystallinity and fewer impurities.[72-73] Vapor-assisted methods have been demonstrated in 3D $CH_3NH_3PbI_3$ perovskites by Liu et al.[74] They used a dual-source thermal evaporation system to evaporate $PbCl_2$ and CH_3NH_3I to produce 3D $CH_3NH_3PbI_3$, which was

much uniform than solution-processed films. The first vapor-assisted method for preparing low-dimensional halide perovskite materials was reported by Guo et al.[73] They fabricated 2D/3D mixed hybrid perovskite thin films by low-pressure vapor-assisted solution process (LP-VASP). The solid-vapor reaction was conducted between spin-coated PEAI-doped PbI_2 thin film and MAI vapor under controlled pressure. Due to the weak van der Waals interaction between organic PEA^+ cation and inorganic octahedral $[PbI_6]$, the vapor MA^+ cation can accessibly intercalate into the octahedral $[PbI_6]$ to form 2D perovskites. They found that the PEAI-doped perovskite films by MAI vapor treatment exhibited a similar absorption with a cut-off at 780 nm, suggesting that the predominant structure of MAI-vapor-$CH_3NH_3PbI_3$ was 3D $CH_3NH_3PbI_3$ rather than 2D $CH_3NH_3PbI_3$

4. Perovskite solar cells by the low-dimensional halide perovskites

4.1 Perovskite solar cells by low n quasi-2D perovskites (n<5)

The low-dimensional halide perovskite materials have been intensively investigated in solar cells application over the last few years.[75] The first PSCs by 2D halide perovskites was reported by Smith *et al.*[44] In this study, the authors systematically investigated the origins of instability in traditional 3D $CH_3NH_3PbI_3$ and proposed a new concept of 2D layered perovskites, which was crafted by using PEAI molecules in place of MAI, as shown in **Figure 1a**. The 2D layered perovskites with a structure of $(PEA)_2(MA)_2Pb_3I_{10}$ (n=3) exhibited a dramatically enhanced moisture stability compared to 3D $CH_3NH_3PbI_3$. However, as indicated in **Figures 1b & 1c**, the PCEs were lower than 5% from PSCs with a device structure of FTO/compact TiO_2/$(PEA)_2(MA)_2Pb_3I_{10}$ (n=3)/spiro-OMeTAD/Au, due to low absorption coefficient and poor carrier transport of $(PEA)_2(MA)_2Pb_3I_{10}$ (n=3). Interestingly, Sargent and his colleagues found that the 2D layered perovskite with $(PEA)_2(MA)_2Pb_nI_{3n+1}$ (n=60) possessed superior long-term

stability, and PSCs by this novel 2D perovskites exhibited decent PCEs.[41] PCEs observed from PSCs based on $(PEA)_2(MA)_2Pb_nI_{3n+1}$ (n=60) were declined from initial 17.21% to 12.80% after 2 weeks, while PCEs from PSCs by 3D $CH_3NH_3PbI_3$ was reduced from initial 16.47% to 0.72% after 2 weeks in humidity air (RH 55%). But these device performances were relatively poor since the insulating organic spacer cations hindered charge transport.[46-47]

Motivated by Smith's work, many researchers have recently focused on the development of alternative and effective spacer cations for balancing PCEs and stability of PSCs.[62, 76] Kanatzidis *et al.* reported a highly oriented 2D perovskite thin films, where n-buthylammonium (n-BA) cation was substituted by PEA cation.[62] The 2D $(n-BA)_2(MA)_2Pb_nI_{3n+1}$ family of perovskite compounds (n=1 to n=4) was synthesized from a stoichiometric reaction between PbI_2, MAI, and n-BA. As shown in **Figures 2a & 2b**, $(n-BA)_2(MA)_2Pb_nI_{3n+1}$ perovskite thin film showed a highly remarkable orientation. In the case of n=1, the $(n-BA)_2(MA)_0Pb_1I_4$ has a preferential growth along the (110) direction, and thus revealed the ($00l$) reflection (crystallizing along the ($hk0$) plane, thereby showing only the ($00l$) reflection). As the n was larger (n>1), the n-BA cations have an intention to confine the perovskite growth within the planar layer, but the MA cations have an intention to expand the perovskite growth outside the layer. For compound as the n=2, the ($0k0$) reflections were split into the (111) and (202) reflections, which indicated that the vertical growth of the compound was pronounced. This effect was more serious for the compounds as n=3 and 4.[62] Noted that the 2D $(n-BA)_2(MA)_2Pb_3I_{10}$ thin films remained stable after 2 months as it was evident from the x-ray diffraction (XRD) spectra shown in **Figures 2c & 2d**. Such enhanced stability was attributed to the hydrophobicity of the long BA cation chain, preventing direct contact of adventitious water within perovskite. PSCs by 2D (n-BA)$_2$(MA)$_2$Pb$_3$I$_{10}$ with a device structure of FTO/TiO$_2$(compact)/TiO$_2$(mesoporous)/(n-

BA)$_2$(MA)$_2$Pb$_3$I$_{10}$/spiro-OMeTAD/Au yielded a PCE of 4.02%. Such a low PCE was majorly attributed to poor charge carrier transport in the vertical transportation since the BA cation with a long chain serves as the potential barriers for charge carrier transporting. To circumvent the above issues, Liang *et al.* designed an alternative 2D perovskites with a short branched-chain, butylamine (iso-BA) spacer cations.[76] The 2D (iso-BA)$_2$(MA)$_3$Pb$_4$I$_{13}$ (n=4) were prepared from precursor solution by mixing PbI$_2$, C$_3$H$_9$NH$_2$, HI, and CH$_3$NH$_3$I at a stoichiometric ratio of 4:2:2:3 in DMF. As shown in **Figure 3a**, compared to the long-linear-chain of n-BA in 2D (n-BA)$_2$(MA)$_3$Pb$_4$I$_{13}$ (n=4), the short-branched-chain of iso-BA in 2D (iso-BA)$_2$(MA)$_3$Pb$_4$I$_{13}$ (n=4) could facilitate charge carrier transporting efficiently in the vertical direction. As a result, PSCs by 2D (iso-BA)$_2$(MA)$_2$Pb$_3$I$_{10}$ with a device structure of FTO/C$_{60}$/iso(-BA)$_2$(MA)$_2$Pb$_3$I$_{10}$/spiro-OMeTAD/Au yielded a PCE of 8.82%, which was over 60% enhancements compared to that (5.38%) by 2D (n-BA)$_2$(MA)$_2$Pb$_3$I$_{10}$ with the same device structure. Moreover, the highest PCEs of 10.63% were observed from PSCs if the 2D (iso-BA)$_2$(MA)$_2$Pb$_3$I$_{10}$ was cast from a hot solution. Such enhanced PCEs were ascribed to the out-of-plane orientation of 2D (iso-BA)$_2$(MA)$_2$Pb$_3$I$_{10}$ thin films from the hot casting method, as indicated in **Figures** 3**b** & 3**c**.

It was reported that the low-dimensional perovskite materials tend to be growth in the direction parallel to the substrates, which hinders the charge transport in the vertical direction. The two-step method in preparation of the low-dimensional perovskite materials was proposed to address the above issues. Mhaisalkar et al. reported a sequential deposition method to fabricate low-dimensional perovskite thin films.[77] The fabrication method was presented in **Figure 4a**. (IC$_2$H$_4$NH$_3$)$_2$PbI$_4$ thin film was first prepared on the substrates by spin-coating method, then the CH$_3$NH$_3$I solution was immersed on the surface of (IC$_2$H$_4$NH$_3$)$_2$PbI$_4$ to form (IC$_2$H$_4$NH$_3$)$_2$(CH$_3$NH$_3$)$_{n-1}$Pb$_n$I$_{3n+1}$ perovskite thin films. The 2D grazing-incidence wide-angle X-

ray scattering (GIWAXS) was used to investigate the crystal orientation of $(IC_2H_4NH_3)_2(CH_3NH_3)_{n-1}Pb_nI_{3n+1}$ thin films, concerning the dipping duration. As indicated in **Figures 4b & 4c,** the crystal orientation of perovskite thin films exhibited preferential crystal orientation in the out-of-plane direction as the dipping duration was last for 5 mins. As a result, the highest PCE of 9.03% was observed from PSCs with a device structure of FTO/TiO$_2$ blocking layer/mesoporous TiO$_2$/$(IC_2H_4NH_3)_2(CH_3NH_3)_{n-1}Pb_nI_{3n+1}$/spiro-OMeTAD/Au.

The charge carrier transport along the out-of-plane direction is more difficult than that from the inorganic layer due to the insulating organic layer. It is accepted that additives could assistant the crystal growth of 2D perovskite films in the vertical direction.[78-79] The first additive used in the preparation of the low dimensional perovskites was demonstrated by Chen and his co-workers.[80] They added ammonium thiocyanate (NH$_4$SCN) into precursor solution containing BAI, PbI$_2$, and MAI, and then prepared perovskite thin films by a one-step method at room temperature.[80] The boundary-free with larger grains oriented in the vertical direction was found in the $(BA)_2(MA)_2Pb_4I_{10}$ (n =3) thin films processed with 1SCN additive (1 is the mole-ratio of NH$_4$SCN to $(BA)_2(MA)_2Pb_4I_{10}$). The perovskite thin films prepared by the above method exhibited enhanced charge carrier mobility.[80] As shown in **Figure 5a-d**, they further fabricated PSCs based on $(PEA)_2(MA)_4Pb_5I_{16}$ (n =5) film processed by different concentrations of NH$_4$SCN, and observed the optimal PCE of 11.01%. Such enhanced PCE was ascribed to the improved charge carrier mobility, vertically orientated 2D perovskite thin films.[81] The crystallization and charge carrier mobility were further improved by NH$_4$SCN cooperated with NH$_4$Cl. A PCE of 14.1% was observed from PSCs by $(PEA)_2(MA)_4Pb_5I_{16}$ (n = 5).[78]

It was also reported that solvent engineering was an effective method in controlling the morphology of quasi-2D perovskite films for achieving high crystallinity in the vertical

direction.[82] Kanatzidis and co‑workers first demonstrated that the mixed DMF and DMSO solvent had a significant influence on the crystallinity, crystal orientation, grain size, and film quality of quasi-2D perovskite films.[83] Gao et al. further explored its working mechanism.[84] It was found that for DMF only solvent, perovskite, and intermediate complex co-exist in the film after anti-solvent treatment, and therefore it has a tendency to grow in different directions after thermal annealing. However, by using DMF:DMSO mixed solvent, there was only one intermediate complex formed after anti-solvent treatment. As a result, the quasi-2D perovskites from DMF:DMSO mixed solvent exhibited highly oriented crystallization. In addition, alternative low polarity and suitable boiling point solvent dimethylacetamide (DMAC) also exhibited a remarkable effect on crystallization kinetics.[85] A mixture of DMF:DMSO: hydriodic acid (HI) has been reported to assist $(3AMP)(MA_{0.75}FA_{0.25})_3Pb_4I_{13}$ film (where AMP is 3‑(aminomethyl)piperidinium) with much more preferred perpendicular orientation and better crystalline quality, yielding PSCs with a PCE of 12.04%.[86]

The cooperation of different large spacer cations was further demonstrated by Chen and his co-workers.[87] Another spacer cation PEAI was added into $BA_2MA_4Pb_5I_{16}$ (n = 5) perovskite precursor solution.[87] They found that PEAI in $BA_2MA_4Pb_5I_{16}$ (n = 5) perovskite precursor solution can assist preferential nucleation and reduce the nucleation density, resulting in perovskite with large grains, and consequently PSCs with high PCEs (a PCE of 14.09 %).

By substitution of the para position of PEA with fluorine, Zhang and his co-workers introduced new organic spacer F-PEA in 2D perovskites.[88] They found that F-PEA can assist perovskite sheets oriented well and enhance π orbital overlapping in the out-of-plane direction, leading to higher out-of-plane conductivity (**Figure 6a-d**). PSCs by F-PEA-based 2D perovskites

with a device structure of FTO/c-TiO$_2$/(F-PEA)$_2$MA$_4$Pb$_5$I$_{16}$/spiro-OMeTAD/Au exhibited a PCE of 13.64% (**Figure 6e**).

The development of efficient organic spacers and understanding the charge transport mechanism are very important to further boost PCEs of PSCs. Xu et al.[89] developed two multiple-ring spacer cations, 1-naphthalenemethylammonium (NpMA) and 9-anthracenemethylammonium (AnMA) for approaching high PCEs from PSCs. As shown in **Figures 7a & 7b**, the absorption and PL spectra of 2D perovskite thin films confirmed that 2D perovskite thin films based on either AnMA or NpMA organic spacers showed similar bandgaps and 3D-like phases. The slightly blue-shifted PL peak observed from 2D perovskite thin films based on NpMA organic spacers, as compared with that based on AnMA organic spacer, indicated that the formation of more layered perovskite phases in the NpMA based 2D perovskite thin films. PSCs with a device structure of glass/ITO/PEDOT:PSS/perovskite/PCBM/BCP/Ag (n is 4) as shown in **Figure 7c** exhibited an ultrahigh open-circuit voltage (V$_{OC}$) of 1.24 V, a large short circuit current density (J$_{SC}$) of 20.89 mA cm^{-2}, a fill factor (FF) of 66.35% and an overall PCE of 17.25% (**Figure 7d**). However, it was found that PSCs fabricated by AnMA based 2D perovskite thin films exhibited a much low PCE of 14.47%. Such poor PCE was attributed to the decreased charge carrier lifetime, enlarged trap density and increased charge carrier nonradiative recombination loss in AnMA based 2D perovskite thin films.

It was further reported that high-quality 2D perovskite thin films with oriented out-of-plane direction can be achieved through the incorporation of a suitable amount of FA$^+$.[90] As shown in **Figure 8a-d**, Zhou et al. found that pristine (BA)$_2$MA$_3$Pb$_4$I$_{13}$ possess highly oriented crystal grain with the (111) planes, which is paralleled to the substrate surface, whereas the

$(BA)_2(MA_{0.8}FA_{0.2})_3Pb_4I_{13}$ thin films exhibited even stronger intensity in the out-of-plane direction. The PSCs by $(BA)_2MA_3Pb_4I_{13}$ thin films showed a PCE of 12.81%.

Zhang et al. reported PSCs by 2D $BA_2(Cs_{0.02}MA_{0.64}FA_{0.34})_4Pb_5I_{16}$ (n = 5), which was based on triple cations (MA^+, FA^+, and Cs^+).[91] The mixed triple cations could induce 2D perovskites with smooth, compact surface morphology, large grain size, and fewer grain boundaries compared to MA-based 2D perovskites. PSCs by 2D $BA_2(Cs_{0.02}MA_{0.64}FA_{0.34})_4Pb_5I_{16}$ (n = 5) showed a PCE of 14.23%. Such enhanced PCE was originated from longer carrier lifetime and higher conductivity of triple cations based 2D perovskite thin films.

The ACI-type 2D perovskites exhibited a reduced bandgap compared to RP perovskites with the same n values, which was due to larger crystal symmetry and different stacking.[92] The first PSCs by ACI 2D perovskite $(Gua)(MA)_nPb_nI_{3n+1}$ (n = 1-3) was reported by Kanatzidis et al. (where Gua is guanidinium), which showed a PCE of 7.26%.[92] The film morphology of $(Gua)(MA)_3Pb_3I_{10}$ (n = 3) and QW's distribution were further tuned with the assistance of MACl additive. As a result, an impressive PCE (18.48%) was observed.[93]

Recent advancement of PSCs by low n quasi-2D mixed perovskites (n<5) is summarized in **Table 1**.

4.2 Perovskite solar cells by 2D/3D mixed perovskites

PSCs based on low n quasi-2D perovskite (n<5) exhibited superior long-term operational stability but possessed poor PCEs compared to pure 3D perovskites. Toward the ends, PSCs based on 2D/3D mixed perovskites were developed to enhance PCEs and boost long-term stability as well.

Zhou et al. reported a two-step method in fabrication of $(PEI_2PbI_4)_x(MAPbI_3)_{1-x}$ perovskite thin film (where x is 2%).[94] which was prepared by spin-coating a mixture solution of PbI_2 and

PEI·HI, and then followed with deposition of an MAI layer through spin-casting method. They found that a small amount of PEI_2PbI_4 can adjust the film morphology and crystallization of perovskite thin film. A PCE of over 15% was demonstrated from $(PEI_2PbI_4)_x(MAPbI_3)_{1-x}$ (x=2%) perovskite thin film. The enhanced device performance was ascribed to the PEI_2PbI_4 doping at the molecular level rather than the merits from the low-dimensional structure.

Later on, Huang et al reported $MAPbI_3$ incorporated with diethylammonium iodide (DAI, $(CH_3CH_2)_2NH_2I$) as an organic spacer.[95] As shown in **Figure 9a**, it was found that the DA mixed perovskite film exhibited stronger diffusion peaks at the (110) and (220) plans, with a smaller full width at half maximum (FWHM) as compared with those from $MAPbI_3$, indicating that these novel perovskite thin films possessed better crystallinity. PSCs based on $(DA_2PbI_4)_{0.05}MAPbI_3$ perovskite thin film exhibited a PCE of 19.05%, which was much higher than that (15.73%) by $MAPbI_3$ thin film (15.73%). The results are shown in **Figure 9b**. The authors believed that enhanced PCEs were mainly ascribed to the large grains and fewer grain boundaries.

To further enhance both PCEs and stability, Chen et al. reported mesoscopic PSCs based on highly stable 2D/3D mixed perovskite $(PEA_2PbI_4)_x(MAPbI_3)$ (where x=0.0017) thin film.[96] As shown in **Figure 10a**, no shift in the 2θ values and no new diffraction peaks from the $(PEA_2PbI_4)_x(MAPbI_3)$ thin film were observed, indicating that a tiny of 2D perovskite was hard to alter the crystal structure of $MAPbI_3$ thin film. Moreover, $(PEA_2PbI_4)_x(MAPbI_3)$ thin-film exhibited blue-shifted absorption and PL spectra (**Figures 10b & 10c**) compared to that of pure $MAPbI_3$ thin film, which is due to the presence of 2D sheet in $(PEA_2PbI_4)_x(MAPbI_3)$ thin film. As shown in **Figure 10d**, PSCs by 2D/3D mixed perovskite $(PEA_2PbI_4)_x(MAPbI_3)$ (where x=0.0017) showed a PCE of 19.84% with a V_{OC} of 1.146 V, J_{SC} of 22.69 mA/cm^2, and FF of

0.7632, respectively. However, PSCs by PEA_2PbI_4 incorporated with a small amount of $MAPbI_3$ exhibited lower J_{SC}.

Most of the work on 2D/3D mixed perovskites was focused on MA cation at the A site. Lately, such an approach was extended to FA as well as to Cs^{1+} cation, and the final goal is to replace toxic lead as well as to maximize the device stability. Wu et al. reported $Cs_{0.1}(FA_{0.83}MA_{0.17})_{0.9}Pb(I_{0.83}Br_{0.17})_3$ incorporated Gua^+ to form CsGuaFAMA mixed cation perovskite.[97] As shown in **Figure 11a**, all of the samples have a similar band edge at ~ 770 nm, which indicated that a tiny amount of Gua^+ does not affect the bandgap of perovskite thin films. But 10% Gua^+ in perovskite thin-film showed the highest PL intensity and then PL intensities were gradually decreased as the concentration of Gua^+ was over 10%, which is due to the formation of 1D $GuaPbI_3$, as illustrated in **Figure 11b**. The time-resolved PL (TRPL) studies (**Figure 11c**) demonstrated that the bi-molecular radiative recombination was gradually enhanced by embedding larger Gua^+ into perovskite thin film. In addition, by incorporating Gua^+, the suppressed defect, elongated PL lifetime, reduced energy disorder in the band edge, enlarged charge recombination resistance, and suppressed trap state density were found in the resultant perovskite thin film. As a result, enlarged V_{OC} from 1.11 V to 1.19 V and consequently an enhanced PCE of 21.12 % was observed.

Recent advancement of PSCs by 2D/3D mixed perovskites is summarized in **Table 2**.

4.3 Perovskite solar cells by 2D/3D perovskites with a bilayer structure

It has been reported that the effective mitigation of defects in perovskite thin films is essential to further enhance the device performance of PSCs. Therefore, the formation of 2D/3D heterojunctions structure is a promising method to improve the perovskite absorber layer with lower defect densities and longer charge carrier lifetimes.

Zhao et al. explored a series of diammonium iodides, $NH_3I(CH_2)_4NH_3I$ (C4), $NH_3I(CH_2)_8NH_3I$ (C8), and $NH_3I(CH_2)_2O(CH_2)_2NH_3I$ (EDBE) (**Figure 12a**) to passivate perovskite surface and grain boundaries.[98] It was found that the molecular structure of diammonium salts has a profound effect on the surface morphology and phase purity of perovskite thin films (**Figure 12b**). Also, C4- and EDBE-caped perovskite thin films showed phase transformation during treatment, which is unfavorable for charge carrier transportation. The C8-caped perovskite thin-film could efficiently passivate perovskite thin film and thus, the C8 salt was used to dope the electron transport layer PCBM. As a result, PSCs by the C8-caped perovskites thin film exhibited a PCE of over 17.60%.

Chen et al. reported an innovative facile way to prepare PEA_2PbI_4 capping layer on the top of 3D $Cs_{0.05}(FA_{0.83}MA_{0.17})_{0.95}Pb(I_{0.83}Br_{0.17})_3$ 3D perovskite thin film.[99] It was found that the PEA_2PbI_4 layer upon 3D perovskite thin film can simultaneously improve the device performance and stability of PSCs by 2D/3D perovskites, as shown in **Figure 13**. PSCs by the 2D/3D perovskites treated by 1 mg/mL PEAI solution showed a PCE of 18.51%, which was ~ 10% enhancement compared to that by 3D perovskites. The enhanced device performance was attributed to the reduced nonradiative recombination loss in the 2D/3D perovskites. Similar work was also reported by Jiang et al.[100] They prepared a PEA_2PbI_4 layer on top of $FA_{1-X}MA_XPbI_3$ thin film to suppress the surface defects of perovskite thin films for approaching efficient PSCs, as shown in **Figures 14a & b**. It was found that a thin PEAI layer can not only stabilize the α phase of $FAPbI_3$, but also can slow down the degradation of underneath 3D perovskite, which was confirmed by both XRD and XPS studies (**Figures 14c & d**). The PSCs by 2D/3D perovskites with a device structure of $ITO/SnO_2/perovskite/spiro-OMeTAD/Au$ shown a PCE of 23.56% with a V_{OC} of 1.16, a J_{SC} of 24.9 mA/cm^2, and a FF of 81.4%.

Recent advancement of PSCs by 2D/3D perovskites with a bilayer structure is summarized in **Table 3**.

5. Perovskite photodetectors by the low-dimensional halide perovskites

PDs refer to light-responsive devices that convert optical signals into electric signals, which is central to modern science and technology because of their great applications, including imaging, vision, and digital display technology.

PDs could catalog as the two-terminal and three-terminal devices based on device architecture. The two-terminal devices are composed of photodiode and photoconductor, and the three-terminal devices refer to phototransistors with source, drain, and gate electrodes. PDs with a two-terminal device structure generally provide a low driving voltage and fast photoresponse owing to a narrow electrode spacing (~ hundreds nanometer). Noted that the photodiodes-based PDs cannot exceed 100% external quantum efficiency (EQE) since no additional charge injection occurs under the reverse bias, but it happens in photoconductor-based PD. The photoconductive gain (G) is given by the ratio of trapped carriers ($\tau_{lifetime}$) to the transit time of the transported carriers ($\tau_{transit}$) through the device. The G is described as $G = \frac{\tau_{lifetime}}{\tau_{transit}}$. Generally, phototransistor-based PDs need a high driving voltage to obtain decent device performance due to their wide electrode space.

Currently, PDs market was mainly dominated by photodiodes based on crystalline inorganic semiconductors, such as silicon, Ge, and InGaAs. However, the preparation of these inorganic PDs was not a cost-effective process. Moreover, some of these inorganic-based PDs are required to be operated at extremely low temperatures, which substantially limits their applications. Thus, it is necessary to develop high-performance PDs with easy manufacturing and cost-effective techniques.

In recent years, the emerging of the low-dimensional halide perovskite single-crystal has attracted tremendous attention in the fabrication of PDs owing to their remarkable optical and electronic properties, such as reduced defects and enhanced charge transfer, compared with the low-dimensional halide perovskite polycrystalline films. However, the challenges in reducing dark current and enhancing photocurrent along the direction of the charge transporting need to be addressed.

Feng and co-workers developed a series of perovskite nanowire (NW) of $(BA)_2(MA)_{n-1}Pb_nI_{3n+1}$ with a pure (101) crystallographic orientation.[101] They found that $(BA)(MA)_{n-1}Pb_nI_{3n+1}$ single-crystal exhibited fewer surface defects and grain boundaries, which allow efficient charge transport in the inorganic layer $[PbI_6]$. In addition, the BA^+ as an insulating organic barrier is responsible for suppressing the dark current and the exotic crystal edges in perovskites are a benefit for efficient exciton dissociation. Thus, $(BA)_2(MA)_3Pb_4I_{13}$ single crystal-based PDs exhibited a high responsivity of $1.5 \times 10^4 \ AW^{-1}$ and a specific detectivity of over 7×10^{15} Jones (cm $Hz^{1/2} W^{-1}$).

Zhu et al. reported large-scale low-dimensional halide perovskite $(C_4H_9NH_3)_2PbBr_4$ by the potassium ions assisted controllable crystal growth during the precipitation process.[102] They found that the $(C_4H_9NH_3)_2PbBr_4$ nanobelts exhibited intense PL and good stability under ambient conditions. The PDs fabricated by dropping the $(C_4H_9NH_3)_2PbBr_4$ nanobelts on the interdigitated Au electrodes exhibited a low dark current of $1.5 \times 10^{-9} \ A$, and photocurrents of $8.21 \times 10^{-8} \ A$ and $6.76 \times 10^{-8} \ A$ at light irradiation under 365 nm and 405 nm, respectively, and under an applied voltage of 5 V. They attributed such high photocurrent to the interconnected network enable better contact with the electrodes, resulting in a better carrier transfer, and the pores

within the $(C_4H_9NH_3)_2PbBr_4$ nanobelts could increase light scattering, leading to the light-harvesting capability for photodetection.

Wang and co-workers reported a high-performance PDs by free-standing $(C_4H_9NH_3)_n(CH_3NH_3)_{n-1}Pb_nI_{3n+1}$ single crystals.[60] The $(C_4H_9NH_3)_n(CH_3NH_3)_{n-1}Pb_nI_{3n+1}$ single crystals were prepared from the water-air interface. The crystallization process occurred through nucleation and crystal growth. The nucleation rate J, is exponentially related to the energy barrier for nucleation, ΔG,[91] which is expressed by an Arrhenius-type equation:[103]

$$J = \Lambda \cdot exp\frac{-\Delta G}{k_B T} \qquad (8)$$

where Λ depends on supersaturation, k_B is the Boltzmann constant, and T is temperature. The energy barrier for nucleation is different in bulk solution and at the water-air interface.

$$\Delta G_{bulk} = \frac{16}{3}\pi\sigma^3 \left(\xi - E_C - \xi_A + k_B T \cdot ln\frac{1}{\frac{M_S^j}{M_A} - J^2 M_S^{j-1}} \right)^{-2} \qquad (9)$$

$$\Delta G_{surface} = \frac{16}{3}\pi\sigma^3 \left(\xi - E_C - \xi_A + \chi + k_B T \cdot ln\frac{1}{\frac{M_S^j}{M_A} - J^2 M_S^{j-1}} \right)^{-2} \qquad (10)$$

where ξ is the cohesive energy of precursor molecules in the cluster, ξ_A is the energy of precursor molecules, σ is the surface tension coefficient, and M_S^j and M_A are the total molar concentrations of solvent and precursor molecules, χ is the increased energy of precursor molecules induced by extra tensile elastic stress at the water-air interface as indicated in **Figure 15c**. Thus, a higher nucleation probability at the water-air surface is expected in contrast to that in the bulk solution. Therefore, in the process of crystallization, the self-assembly $C_4H_9NH_3^+$ precursor cation at the water-air interface acts as a soft template helping the growth of nanostructures. The higher solvation energy of precursor molecules at the asymmetric water-air

interface offers higher chemical potentials, leading to a low energy barrier and faster in-plane growth. Consequently, inch-size freestanding quasi-2D perovskite single crystals have been achieved at the water-air interface.[60] The PDs based on the quasi-2D perovskite single crystals with the smallest quantum well thickness (n = 1) exhibited a strikingly low dark current of $\sim 10^{-13}$ A, higher on/off ratio of $\sim 10^4$, and faster rise time of ~ 1.7 μs and drop time of 3.9 μs.[60]

Similar work was reported by Liu and co-workers.[104] They synthesized high-quality 36 mm sized 2D $(PEA)_2PbI_4$ by inducing extra surface tension. As shown in **Figure 16b**, the XRD patterns indicated that the top plane and side plane was well-defined with the (001) series and the (010) series of reflections, respectively. They found that PDs by the (001) plane of $(PEA)_2PbI_4$ exhibited better photoresponse compared to that by the (010) plane, with a dramatically low dark current of 3.06×10^{-12} A under a bias of 5 V. Such low dark current was ascribed to boundary-free of $(PEA)_2PbI_4$ single crystals. The $(PEA)_2PbI_4$ based PDs possessed the highest detectivity of 1.89×10^{15} Jones under a bias of 5 V, which was a record-high sensitivity for perovskite PDs.

Recent advancement of perovskite PDs by the low-dimensional perovskites is summarized in **Table 4**.

6. Perovskite light-emitting diodes by the low-dimensional halide perovskites

It was reported that perovskite LEDs based on quasi-2D perovskites could display better device performance than that by 3D counterparts.[105-107] Emma et al. reported a solution-state synthetic route to fabricate well-defined and single-phase white light emitters.[105] They demonstrated that layered $PbBr_2$ perovskites crystals of N1-methylethane-1,2-diammonium (N-MEDA)$[PbBr_4]$ and N1-methylpropane-1,3-diammonium (N-MPDA) $[PbBr_4]$ formed the <110> and <001> oriented structures. The <001> sheets displayed sharp blue emission at approximately 420 nm, whereas the <110> sheets showed broad white-light emission (maximum at 558 nm,

PLQY $\approx$ 0.5%) covering the whole visible spectrum, as shown in **Figure 17a-d**. Thus, a broader emission within the entire visible spectrum was observed from corrugated lead halide sheets in (N-MEDA)[PbBr$_4$] 2D perovskite. Through changing the ligands from N-MEDA to EDBE, they reported "warm" and "cold" white-light-emitting crystals with quantum efficiencies of 2 % and 9 % from perovskite LEDs based on perovskites with Cl and Br anions.[106] Their observations offered a flexible platform for studying the phenomenon of broadband emission from 2D perovskite materials.

In the PEA$_2$(MA)$_{n-1}$Pb$_n$Br$_{3n+1}$ (n = 1-4) system, Byu et al. demonstrated that the quasi-2D perovskites displayed a much higher current efficiency and luminance than 3D MAPbBr$_3$ and 2D PEA$_2$PbBr$_4$.[108] They reported a series of precursor solutions with different MA:PEA ratios to prepare PEA$_2$(MA)$_{n-1}$Pb$_n$Br$_{3n+1}$ thin films. As indicated in **Figure 18**, it was found that perovskite LEDs based on the quasi-2D perovskite thin film with MAPbBr$_3$:(PEA)$_2$PbBr$_4$ of 1:16 presented the highest current efficiency and luminance of 4.90 cd/A and 2935 cd/m^2, respectively. Perovskite LEDs were with a device structure of ITO/Buf-HIL/perovskite/TPBI/LiF/Al, where Buf-HIL is poly(3,4-ethylenedioxythiophene):poly(styrene sulfonate): perfluorinated ionomer and TPBI is 1,3,5-tris (N -phenylbenzimiazole-2-yl)benzene.

The iodide-based analog PEA$_2$(MA)$_{n-1}$Pb$_n$I$_{3n+1}$ (n = 5) has been demonstrated by Sargent and co-workers to outperform 3D MAPbI$_3$ (n = ∞) for near-infrared emission, with an EQE of 8.8% and radiance of 80 W sr^{-1} m^{-2}.[109] They further ascribed the superior performance to a cascading energy transfer that funnels photoexcitation to the lowest-bandgap phase within mixed quasi-2D perovskite thin film.

Huang and co-workers demonstrated quasi-2D perovskite LEDs based on (NMA)$_2$(FAPbI$_3$)$_{n-1}$Pb$_n$I$_{3n+1}$, where NMA is naphthylmethyl ammonium, with a recorded EQE of 11.7% and

radiance of 82 W sr^{-1} m^{-2}.[110] Similarly, they attributed the superior device performance to the funneling mechanism, which occurs within sub-ns timescales and outcompetes nonradiative exciton quenching and increases radiative recombination.

Liao and co-workers developed perovskite LEDs exhibiting a deep blue emission with commission international de L'Eclarage (CIE) coordinate at (0.14, 0.05) by designing a new aromatic polyammonium bromide spacer [1, 4-bis(aminomethyl)benzene bromide (P-PDABr$_2$)] with double functional amido terminals, which provided a strong binding force with PbBr$_6$, leading to stable low-dimensional domains.[111] A mixed spacer system (PEABr+P-PDABr$_2$) was further executed to modulate the domain distribution in perovskite film. It was stated that the nonradiative recombination and retarded exciton transfer were significantly suppressed by this method. The device presented a peak EQE of 2.6%, which was an invigorative result for deep blue perovskite LED on basis of pure bromide perovskite.

To enhance radiative emission processes in LEDs, Di and co-workers reported LEDs with a record EQE of 20.1%, by embedding the quasi-2D perovskites (NMA)$_2$(FA)Pb$_2$I$_7$ into a high bandgap polymer poly(2-hydroxyethyl methacrylate) (poly-HEMA) forming a bulk heterojunction (BHJ) composite, where NMA is 1-naphthylmethylammonium.[112] The GIWAXS indicated that the 2D/3D perovskite crystallites were iso-tropically oriented in the perovskite-polymer (PP) BHJ thin film (**Figure 19a**). The LED was constructed from a solution-processed method with a structure of ITO/MZO/PEIE/PPBHJ/TFB-PFO/MoO$_x$/Au, where MZO is magnesium-alloyed zinc oxide, PEIE is polyethylenimine, TFB-PFO is poly(9,9-dioctylfluorene-alt-N-(4-sec-butylphenyl)-diphenylamine) (TFB) blended with poly(9,9-di-n-octylfluorenyl2,7-diyl) (PFO). As indicated in **Figure 19b**, the peak of EQE reached 20.1%, which was a record for perovskite LEDs so far.

Recent advancement in perovskite LEDs based on the low-dimensional perovskites is summarized in **Table 5**.

7. Perovskite lasers by the low-dimensional halide perovskites

A laser refers to a device that can emit coherent light with strong intensity and perfect directionality. By taking into consideration of high absorption coefficient and low density of defects, low-dimensional halide perovskites are excellent gain materials for the development of high-performance lasing devices.

Li et al. demonstrated that FA-based 2D Ruddlesden–Popper perovskites thin films of $(NMA)_2(FA)_{n-1}Pb_nX_{3n+1}$ showed superior optical gain properties.[113] Different from the stimulated emission mechanism of 3D perovskites with electron-hole plasma at room temperature, 2D Ruddlesden–Popper perovskites exhibited the feature of strongly bound electron-hole pairs (excitons) and naturally form an energy cascade. It was observed that amplified spontaneous emission (ASE) from these perovskites with a low threshold ($<20.0 \pm 2$ $\mu J \cdot cm^{-2}$), tunable wavelengths from visible to the near-infrared spectral range (530–810 nm), and good photostability with an operation duration exceeding 1.2×10^8 laser pulses.

After that, Zhang et al. demonstrated room-temperature ASE and lasing from mixed multiple QWs in 2D‐RPPs of $(BA)_2(MA)_{n-1}Pb_nBr_{3n+1}$.[114] They performed femtosecond transient absorption (TA) characterization to reveal an ultrafast population transfer along the energy cascade from small‐n‐QW to large‐n‐QW, concentrating photo excitations at the lowest bandgap QWs ($n \approx \infty$), enabling the population inversion for stimulated emission. They found that the 2D-RPPs of $(BA)_2(MA)_5Pb_6Br_{19}$ (n=6) show an ASE threshold of 13.6 μJ cm^{-2} and a high gain coefficient (G) of 112 cm^{-1}. Their findings reveal that 2D RPPs can be potentially applied for electrically driven lasers in on‐chip integration of photonics and electronic circuits.

Recent advancement of perovskite lasers based on the low-dimensional perovskites is summarized in **Table 6**.

8. Summary and outlook

The emergence of low-dimensional perovskites as semiconductors has revolutionized next-generation optoelectronics owing to their extraordinary optical and electronic properties. In this short review, we discussed the optoelectronic properties of the low-dimensional halide perovskites. From this point of view, we highlighted the properties of 2D perovskite MQWs structure. The decrease in the value of n could lead to a compression of exciton wavefunction in the QW due to dielectric confinement, which results in enhanced exciton binding energy within 2D perovskites. In addition, the observation of charge carrier density at the ES is close to that of metal, which implies that the low-dimensional perovskites offer great opportunities for designing novel optoelectronics. Subsequently, we reviewed synthetic methods for the preparation of the low-dimensional halide perovskites, including the one-pot synthetic method, direct growth method, polar solvents free method, and vapor-assisted method. Despite the great progress in the synthetic methods for the preparation of low-dimensional halide perovskites, more work needs to be done in the future towards the understanding of the crystal nucleation and growth mechanism, aiming to achieve ultra-uniform low-dimensional perovskite thin films.

The low-dimensional perovskites with nontrivial optical and electronic properties display tremendous potential applications in solar cells, PDs, LEDs, and lasers. To further explore the unique characteristics of the low-dimensional perovskites for all these applications, more research is demanded to focus on materials design and the fundamental physical and chemical properties of the low-dimensional perovskites.

In terms of PSCs by the low-dimensional perovskites, even though enormous efforts have been devoted to approaching the vertical orientation of perovskite thin films, aiming to accelerate the charge carrier transport in the vertical direction, the efficiencies were still hard to compete with those by 3D perovskites. To overcome it, we think that we should establish the judicious selection criteria for organic spacer's design principles for 2D perovskites, for example, the effect of different spacer lengths, functional units, and the substituent groups; It is necessary to develop low-dimensional perovskite structures with pure phases, like adopting mechanical exfoliation process, to avoid the drawbacks of the anisotropic properties. The synthetic techniques and characterization are required to study the optical and electronic properties of 2D perovskites, and a deep understanding of structure-property relationships of different 2D perovskite phases needs to be explored. To substitute the insulating organic spacers with conjugated organic spacers would be a fascinating direction for boosting PCEs of PSCs, In addition, forming low bandgap organic donor (or acceptor)/2D perovskite bulk heterostructure would not only contribute to additional absorption of the 2D perovskite but also minimize the energy required for dissociating exciton into free charge carriers.

For perovskite PDs by the low-dimensional perovskites, great efforts are still demanded to achieve high device performance. To minimize the dark current in perovskite PDs by the low-dimensional perovskites, surface passivation between the low-dimensional perovskites and charge transport layers, utilization of Lewis acid and/or Lewis base to passivate PbX^{3-} and/or Pb^{2+} anti-site defects, and synthesis of the low-dimensional perovskite single crystals (no grain boundary effect) are crucial importance to reduce trap states, which is also essential to achieve high response speed.

Although low-dimensional perovskites are being considered for making next-generation LEDs and lasers in the future, there are some significant challenges. For example, the stronger exciton-lattice coupling and randomly oriented polycrystalline in the low-dimensional perovskite thin films are responsible for fast nonradiative exciton quenching. Toward the ends, large-scale size single-crystalline perovskite films with higher carrier mobility, lower defect density, are expected to replace the conventional polycrystalline perovskite films. It has been reported that the additives can not only effectively passivate perovskite surface traps, but also tune the film morphology, which thus ensures reduced nonradiative recombination.[115] Another effort should be focused on increasing PLQY by metal ions doping and defect passivation with different ligands. Through these novel designs, we would expect to develop devices with high performance by the low-dimensional perovskites in the future.

Conflict of Interest

We declare that we have no competing financial interest, and all the financial support has been acknowledged in the manuscript.

Abbreviations

3D	Three dimensional
2D	Two dimensional
PV	Photovoltaics
PLQY	Photoluminescence quantum yield
PDs	Photodetectors
LEDs	Light-emitting diodes
PCEs	Power conversion efficiencies
PPDs	Perovskite photodetectors
PSCs	Perovskite solar cells
PEA	phenethylammonium ($C_8H_9NH_3$)
MA	Methylammonium (CH_3NH_3)
RP	Ruddlesden-Popper
DJ	Dion-Jacobson
MQWs	Multiple quantum well
ES	Edge states
E_g	Bandgap
VB	Valence band
CB	Conduction band
PA	Phenylammonium
PMA	N-phenylmethylammonium
DPA	N,N -dimethylphenylammounium
PTA	Phenyltrimethylammonium
ALA	Allylammonium
DMF	Dimethylformamide
OLM	Oleylamine
OLA	Oleic acid
LP-VASP	The low-pressure vapor-assisted solution process
XRD	X-ray diffraction
n-BA	n-buthylammonium ($C_4H_{12}N$)
Iso-BA	Iso-buthylammonium ($C_4H_{12}N$)
GIWAXS	Grazing-incidence wide-angle X-ray scattering
NpMA	1-naphthalenemethylammonium
AnMA	9-anthracenemethylammonium
J_{SC}	Short circuit current density
V_{OC}	Open circuit voltage
FF	Fill factor
PL	Photoluminescence
3AMP	3-(aminomethyl)piperidinium
FA	Formamidine
ACI	Alternating cations in the interlayer space
Gua	Guanidinium
BEA	1,4-butanediamine
DAI	Diethylammonium iodide
FWHM	Full width at half maximum

C4	$NH_3I(CH_2)_4NH_3I$
C8	$NH_3I(CH_2)_8NH_3I$
EDBE	$NH_3I(CH_2)_2O(CH_2)_2NH_3I$
EQE	External quantum efficiency
NW	Nanowire
N-MEDA	N1-methylethane-1, 2-diammonium
N-MPDA	N1-methylpropane-1,3-diammonium
TPBI	1,3,5-tris (N -phenylbenzimiazole-2-yl)benzene
NMA	Naphthylmethyl ammonium
P-PDABr$_2$	1,4-bis(aminomethyl)benzene bromide
MZO	Magnesium-alloyed zinc oxide
PEIE	Polyethylenimine
TFB	Poly(9,9-dioctylfluorene-alt-N-(4-sec-butylphenyl)-diphenylamine)
PFO	Poly(9,9-di-n-octylfluorenyl2,7-diyl
HEA	2-hydroxyethylamine
ThMA	2-thienylmethylammonium
NPA	N-(2-Bromoethyl)-1,3-propanediamine
NMA	1-naphthylmethylamine

References

1. Kojima A, Teshima K, Shirai Y, et al. Organometal halide perovskites as visible-light sensitizers for photovoltaic cells. *J. Am. Chem. Soc.* 2009;**131**:6050-6051.

2. Lee M M, Teuscher J, Miyasaka T, et al. Efficient hybrid solar cells based on meso-superstructured organometal halide perovskites. *Science* 2012;**338**:643-647.

3. Jeon N J, Noh J H, Kim Y C, et al. Solvent engineering for high-performance inorganic–organic hybrid perovskite solar cells. *Nat. Mater.* 2014;**13**:897-903.

4. Burschka J, Pellet N, Moon S-J, et al. Sequential deposition as a route to high-performance perovskite-sensitized solar cells. *Nature* 2013;**499**:316-319.

5. Stoumpos C C, Malliakas C D.Kanatzidis M G. Semiconducting tin and lead iodide perovskites with organic cations: phase transitions, high mobilities, and near-infrared photoluminescent properties. *Inorg. Chem.* 2013;**52**:9019-9038.

6. Heo J H, Im S H, Noh J H, et al. Efficient inorganic-organic hybrid heterojunction solar cells containing perovskite compound and polymeric hole conductors. *Nat. Photonics* 2013;**7**:486.

7. Snaith H J. Perovskites: the emergence of a new era for low-cost, high-efficiency solar cells. *J. Phys. Chem.* 2013;**4**:3623-3630.

8. Calado P, Telford A M, Bryant D, et al. Evidence for ion migration in hybrid perovskite solar cells with minimal hysteresis. *Nat. Commun.* 2016; **7**:1-10.

9. Hodes G.Cahen D. Photovoltaics: perovskite cells roll forward. *Nat. Photonics* 2014;**8**:87-88.

10. Wang K, Zheng L, Zhu T, et al. High performance perovskites solar cells by hybrid perovskites Co-crystallized with poly (ethylene oxide). *Nano Energy* 2020;**67**:104229.

11. Wang K, Zheng L, Zhu T, et al. Efficient perovskite solar cells by hybrid perovskites incorporated with heterovalent neodymium cations. *Nano Energy* 2019;**61**:352-360.

12. Xu W, Zheng L, Zhu T, et al. Bulk heterojunction perovskite solar cells incorporated with zn_2sno_4 nanoparticles as the electron acceptors. *ACS Appl. Mater. Interfaces* 2019;**11**:34020-34029.

13. Dou L, Yang Y M, You J, et al. Solution-processed hybrid perovskite photodetectors with high detectivity. *Nat. Commun.* 2014;**5**:1-6.

14. Zhu T, Yang Y, Zheng L, et al. Solution‐processed flexible broadband photodetectors with solution‐processed transparent polymeric electrode. *Adv. Funct. Mater.* 2020;1909487.

15. Liu C, Wang K, Du P, et al. Ultrasensitive solution-processed broad-band photodetectors using $CH_3NH_3PbI_3$ perovskite hybrids and PbS quantum dots as light harvesters. *Nanoscale Res. Lett.* 2015;**7**:16460-16469.

16. Xu W, Guo Y, Zhang X, et al. Room-temperature-operated ultrasensitive broadband photodetectors by perovskite incorporated with conjugated polymer and single-wall carbon nanotubes. *Adv. Funct. Mater.* 2018;**28**:1705541.

17. Van Le Q, Jang H W.Kim S Y. Recent advances toward high-efficiency halide perovskite light‐emitting diodes: review and perspective. *Small Methods* 2018;**2**:1700419.

18. Zhang X, Liu H, Wang W, et al. Hybrid perovskite light‐emitting diodes based on perovskite nanocrystals with organic-inorganic mixed cations. *Adv. Mater.* 2017;**29**:1606405.

19. Wang J, Wang N, Jin Y, et al. Interfacial control toward efficient and low-voltage perovskite light-emitting diodes. *Adv. Mater.* 2015;**27**:2311-2316.

20. Kumawat N K, Gupta D.Kabra D. Recent advances in metal halide-based perovskite light–emitting diodes. *Energy Technol.* 2017;**5**:1734-1749.

21. Zhang Q, Su R, Du W, et al. Advances in small perovskite-based lasers. *Small Methods* 2017;**1**:1700163.

22. Stylianakis M M, Maksudov T, Panagiotopoulos A, et al. Inorganic and hybrid perovskite based laser devices: a review. *Mater.* 2019;**12**:859.

23. Zhou H, Chen Q, Li G, et al. Interface engineering of highly efficient perovskite solar cells. *Science* 2014;**345**:542-546.

24. Wang K, Liu C, Du P, et al. Bulk heterojunction perovskite hybrid solar cells with large fill factor. *Energy Environ. Sci.* 2015;**8**:1245-1255.

25. https://www.nrel.gov/pv/assets/pdfs/best-research-cell-efficiencies.20190802.pdf.(Accessed: Aug. 2nd.

26. Liu C, Wang K, Du P, et al. High performance planar heterojunction perovskite solar cells with fullerene derivatives as the electron transport layer. *ACS Appl. Mater. Interfaces* 2015;**7**:1153-1159.

27. Zheng L, Wang K, Zhu T, et al. Solution-processed ultrahigh detectivity photodetectors by hybrid perovskite incorporated with heterovalent neodymium cations. *ACS omega* 2019;**4**:15873-15878.

28. Luo C, Li W, Xiong D, et al. Surface pre-optimization of a mixed halide perovskite toward high photoluminescence quantum yield in the blue spectrum range. *Nanoscale* 2019;**11**:15206-15215.

29. Zhu H, Fu Y, Meng F, et al. Lead halide perovskite nanowire lasers with low lasing thresholds and high quality factors. *Nat. Mater.* 2015;**14**:636-642.

30. Conings B, Drijkoningen J, Gauquelin N, et al. Intrinsic thermal instability of methylammonium lead trihalide perovskite. *Adv. Energy Mater.* 2015;**5**:1500477.

31. Niu G, Guo X.Wang L. Review of recent progress in chemical stability of perovskite solar cells. *J. Mater. Chem. A* 2015;**3**:8970-8980.

32. Bartel C J, Sutton C, Goldsmith B R, et al. New tolerance factor to predict the stability of perovskite oxides and halides. *Sci. Adv.* 2019;**5**:eaav0693.

33. Bai Y, Dong Q, Shao Y, et al. Enhancing stability and efficiency of perovskite solar cells with crosslinkable silane-functionalized and doped fullerene. *Nat. Commun.* 2016;**7**:1-9.

34. Zhou S, Zhu T, Zheng L, et al. A zwitterionic polymer as an interfacial layer for efficient and stable perovskite solar cells. *RSC Adv.* 2019;**9**:30317-30324.

35. Zhang F, Shi W, Luo J, et al. Isomer‑pure bis‑PCBM‑assisted crystal engineering of perovskite solar cells showing excellent efficiency and stability. *Adv. Mater.* 2017;**29**:1606806.

36. Krishna A, Gottis S, Nazeeruddin M K, et al. Mixed dimensional 2D/3D hybrid perovskite absorbers: the future of perovskite solar cells? *Adv. Funct. Mater.* 2019;**29**:1806482.

37. Li Z, Yang M, Park J-S, et al. Stabilizing perovskite structures by tuning tolerance factor: formation of formamidinium and cesium lead iodide solid-state alloys. *Chem. Mater.* 2016;**28**:284-292.

38. Bella F, Griffini G, Correa-Baena J-P, et al. Improving efficiency and stability of perovskite solar cells with photocurable fluoropolymers. *Science* 2016;**354**:203-206.

39. Pedesseau L, Sapori D, Traore B, et al. Advances and promises of layered halide hybrid perovskite semiconductors. *ACS Nano* 2016;**10**:9776-9786.

40. Even J, Pedesseau L.Katan C. Understanding quantum confinement of charge carriers in layered 2D hybrid perovskites. *Chemphyschem* 2014;**15**:3733-3741.

41. Quan L N, Yuan M, Comin R, et al. Ligand-stabilized reduced-dimensionality perovskites. *J. Am. Chem. Soc.* 2016;**138**:2649-2655.

42. Etgar L. The merit of perovskite's dimensionality; can this replace the 3D halide perovskite? *Energy Environ. Sci.* 2018;**11**:234-242.

43. Cheng P, Xu Z, Li J, et al. Highly efficient ruddlesden–popper halide perovskite $PA_2MA_4Pb_5I_{16}$ Solar Cells. *ACS Energy Lett.* 2018;**3**:1975-1982.

44. Smith I C, Hoke E T, Solis-Ibarra D, et al. A layered hybrid perovskite solar-cell absorber with enhanced moisture stability. *Angew. Chem. Int. Ed.* 2014;**53**:11232-11235.

45. Song Z, Abate A, Watthage S C, et al. perovskite solar cell stability in humid air: partially reversible phase transitions in the PbI_2-CH_3NH_3I-H_2O system. *Adv. Energy Mater.* 2016;**6**:1600846.

46. Hong X, Ishihara T.Nurmikko A. Dielectric confinement effect on excitons in PbI_4-based layered semiconductors. *Phys. Rev. B* 1992; **45**: 6961.

47. Ishihara T, Takahashi J.Goto T. Optical properties due to electronic transitions in two-dimensional semiconductors $(C_nH_{2n+1}NH_3)_2PbI_4$. *Phys. Rev. B* 1990;**42**:11099.

48. Era M, Morimoto S, Tsutsui T, et al. Organic-inorganic heterostructure electroluminescent device using a layered perovskite semiconductor $(C_6H_5C_2H_4NH_3)_2PbI_4$. *Appl. Phys. Lett.* 1994;**65**:676-678.

49. Jagielski J, Kumar S, Yu W-Y, et al. Layer-controlled two-dimensional perovskites: Synthesis and optoelectronics. *J. Mater. Chem. C* 2017;**5**:5610-5627.

50. Stoumpos C C, Cao D H, Clark D J, et al. Ruddlesden–Popper hybrid lead iodide perovskite 2D homologous semiconductors. *Chem. Mater.* 2016;**28**:2852-2867.

51. Stoumpos C C, Soe C M M, Tsai H, et al. High members of the 2D Ruddlesden-Popper halide perovskites: synthesis, optical properties, and solar cells of $(CH_3(CH_2)_3NH_3)_2(CH_3NH_3)_4Pb_5I_{16}$. *Chem.* 2017;**2**:427-440.

52. Ghosh D, Acharya D, Zhou L, et al. Lattice Expansion in hybrid perovskites: effect on optoelectronic properties and charge carrier dynamics. *J. Phys. Chem.* 2019;**10**:5000-5007.

53. Venkatesan N R, Labram J G.Chabinyc M L. Charge-carrier dynamics and crystalline texture of layered Ruddlesden–Popper hybrid lead iodide perovskite thin films. *ACS Energy Lett.* 2018;**3**:380-386.

54. Blancon J-C, Stier A V, Tsai H, et al. Scaling law for excitons in 2D perovskite quantum wells. *Nat. Commun.* 2018;**9**:1-10.

55. Yaffe O, Chernikov A, Norman Z M, et al. Excitons in ultrathin organic-inorganic perovskite crystals. *Phys. Rev. B* 2015;**92**:045414.

56. Wang K, Wu T, Wu C, et al. Nature of terrace edge states (TES) in lower-dimensional halide perovskite. *J. Mater. Chem. A* 2020;**8**:7659-7670.

57. Peng L, Yuan Y, Li G, et al. Observation of topological states residing at step edges of WTe_2. *Nat. Commun.* 2017;**8**:1-7.

58. Blancon J-C, Tsai H, Nie W, et al. Extremely efficient internal exciton dissociation through edge states in layered 2D perovskites. *Science* 2017;**355**:1288-1292.

59. Wang K, Wu C, Jiang Y, et al. Distinct conducting layer edge states in two-dimensional (2D) halide perovskite. *Sci. Adv.* 2019;**5**:eaau3241.

60. Wang K, Wu C, Yang D, et al. Quasi-two-dimensional halide perovskite single crystal photodetector. *ACS Nano* 2018;**12**:4919-4929.

61. Wang S, Gong Z, Li G, et al. The strain effects in 2D hybrid organic–inorganic perovskite microplates: bandgap, anisotropy and stability. *Nanoscale* 2020;**12(12)**:6644-6650.

62. Cao D H, Stoumpos C C, Farha O K, et al. 2D homologous perovskites as light-absorbing materials for solar cell applications. *J. Am. Chem. Soc.* 2015;**137(24)**:7843-7850.

63. Li Z, Liu N, Meng K, et al. A new organic interlayer spacer for stable and efficient 2D ruddlesden–popper perovskite solar cells. *Nano Lett.* 2019;**19**:5237-5245.

64. Fu W, Liu H, Shi X, et al. Tailoring the functionality of organic spacer cations for efficient and stable quasi‑2D perovskite solar cells. *Adv. Funct. Mater.* 2019;**29**:1900221.

65. Mao L, Stoumpos C C.Kanatzidis M G. Two-dimensional hybrid halide perovskites: principles and promises. *J. Am. Chem. Soc.* 2018;**141**:1171-1190.

66. Proppe A H, Quintero-Bermudez R, Tan H, et al. Synthetic control over quantum well width distribution and carrier migration in low-dimensional perovskite photovoltaics. *J. Am. Chem. Soc.* 2018;**140**:2890-2896.

67. Tyagi P, Arveson S M.Tisdale W A. Colloidal organohalide perovskite nanoplatelets exhibiting quantum confinement. *J. Phys. Chem.* 2015;**6(10)**:1911-1916.

68. Yuan Z, Shu Y, Tian Y, et al. A facile one-pot synthesis of deep blue luminescent lead bromide perovskite microdisks. *Chem. Commun.* 2015;**51(91)**:16385-16388.

69. Dou L, Wong A B, Yu Y, et al. Atomically thin two-dimensional organic-inorganic hybrid perovskites. *Science* 2015;**349(6255)**:1518-1521.

70. Aharon S.Etgar L. Two dimensional organometal halide perovskite nanorods with tunable optical properties. *Nano Lett.* 2016;**16(5)**:3230-3235.

71. Vybornyi O, Yakunin S.Kovalenko M V. Polar-solvent-free colloidal synthesis of highly luminescent alkylammonium lead halide perovskite nanocrystals. *Nanoscale* 2016;**8(12)**:6278-6283.

72. Jiang P, Deng W, Zhou X, et al. Vapor-assisted synthesis of hierarchical porous graphitic carbon materials towards energy storage devices. *J. Power Sources* 2019;**425**:10-16.

73. Li M H, Yeh H H, Chiang Y H, et al. Highly efficient 2D/3D hybrid perovskite solar cells via low-pressure vapor-assisted solution process. *Adv. Mater.* 2018;**30(30)**:1801401.

74. Liu M, Johnston M B.Snaith H J. Efficient planar heterojunction perovskite solar cells by vapour deposition. *Nature* 2013;**501(7467)**:395-398.

75. Tsai H, Nie W, Blancon J C, et al. High-efficiency two-dimensional Ruddlesden–Popper perovskite solar cells. *Nature* 2016;**536(7616)**:312-316.

76. Chen Y, Sun Y, Peng J, et al. Tailoring organic cation of 2D air-stable organometal halide perovskites for highly efficient planar solar cells. *Adv. Energy Mater.* 2017;**7(18)**:1700162.

77. Koh T M, Shanmugam V, Schlipf J, et al. Nanostructuring mixed-dimensional perovskites: a route toward tunable, efficient photovoltaics. *Adv. Mater.* 2016;**28(19)**:3653-3661.

78. Fu W, Wang J, Zuo L, et al. Two-dimensional perovskite solar cells with 14.1% power conversion efficiency and 0.68% external radiative efficiency. *ACS Energy Lett.* 2018;**3**:2086-2093.

79. Qing J, Liu X K, Li M, et al. Aligned and graded type-II Ruddlesden–Popper perovskite films for efficient solar cells. *Adv. Energy Mater.* 2018;**8**:1800185.

80. Zhang X, Wu G, Yang S, et al. Vertically oriented 2D layered perovskite solar cells with enhanced efficiency and good stability. *Small* 2017;**13**:1700611.

81. Zhang X, Wu G, Fu W, et al. Orientation regulation of phenylethylammonium cation based 2D perovskite solar cell with efficiency higher than 11%. *Adv. Energy Mater.* 2018;**8**:1702498.

82. Lian X, Chen J, Zhang Y, et al. Two-dimensional inverted planar perovskite solar cells with efficiency over 15% via solvent and interface engineering. *J. Mater. Chem. A* 2019;**7**:18980-18986.

83. Soe C M M, Nie W, Stoumpos C C, et al. Understanding film formation morphology and orientation in high member 2D Ruddlesden–Popper perovskites for high-efficiency solar cells. *Adv. Energy Mater.* 2018;**8**:1700979.

84. Gao L, Zhang F, Xiao C, et al. Improving charge transport via intermediate-controlled crystal growth in 2D perovskite solar cells. *Adv. Funct. Mater.* 2019;**29**:1901652.

85. Qiu J, Zheng Y, Xia Y, et al. Rapid crystallization for efficient 2D Ruddlesden–Popper (2DRP) perovskite solar cells. *Adv. Funct. Mater.* 2019;**29**:1806831.

86. Ke W, Mao L, Stoumpos C C, et al. Compositional and solvent engineering in Dion–Jacobson 2D perovskites boosts solar cell efficiency and stability. *Adv. Energy Mater.* 2019;**9**:1803384.

87. Lian X, Chen J, Qin M, et al. The second spacer cation assisted growth of a 2D perovskite film with oriented large grain for highly efficient and stable solar Cells. *Angew. Chem. Int. Ed.* 2019;**58**:9409-9413.

88. Zhang F, Kim D H, Lu H, et al. Enhanced charge transport in 2D perovskites via fluorination of organic cation. *J. Am. Chem. Soc.* 2019;**141**:5972-5979.

89. Xu Z, Lu D, Liu F, et al. Phase distribution and carrier dynamics in multiple-ring aromatic spacer-based two-dimensional Ruddlesden–Popper perovskite solar cells. *ACS Nano* 2020;**14**:4871-4881.

90. Zhou N, Shen Y, Li L, et al. Exploration of crystallization kinetics in quasi two-dimensional perovskite and high performance solar cells. *J. Am. Chem. Soc.* 2018;**140**:459-465.

91. Gao L, Zhang F, Chen X, et al. Enhanced charge transport by incorporating formamidinium and cesium cations into two - dimensional perovskite solar cells. *Angew. Chem.* 2019;**131**:11863-11867.

92. Soe C M M, Stoumpos C C, Kepenekian M, et al. New type of 2D perovskites with alternating cations in the interlayer space,$(C(NH_2)_3)(CH_3NH_3)_nPb_nI_{3n+1}$: Structure, properties, and photovoltaic performance. *J. Am. Chem. Soc.* 2017;**139**:16297-16309.

93. Luo T, Zhang Y, Xu Z, et al. Compositional control in 2D perovskites with alternating cations in the interlayer space for photovoltaics with efficiency over 18%. *Adv. Mater.* 2019;**31**:1903848.

94. Yao K, Wang X, Li F, et al. Mixed perovskite based on methyl-ammonium and polymeric-ammonium for stable and reproducible solar cells. *Chem. Commun.* 2015;**51(84)**:15430-15433.

95. Huang X, Cui Q, Bi W, et al. Two-dimensional additive diethylammonium iodide promoting crystal growth for efficient and stable perovskite solar cells. *RSC Adv.* 2019;**9**:7984-7991.

96. Chen J, Lee D.Park N-G. Stabilizing the Ag electrode and reducing J–V hysteresis through suppression of iodide migration in perovskite solar cells. *ACS Appl. Mater. Interfaces* 2017; **9**: 36338-36349.

97. Wu S, Li Z, Zhang J, et al. Efficient large guanidinium mixed perovskite solar cells with enhanced photovoltage and low energy losses. *Chem. Commun.* 2019;**55**:4315-4318.

98. Zhao T, Chueh C-C, Chen Q, et al. Defect passivation of organic–inorganic hybrid perovskites by diammonium iodide toward high-performance photovoltaic devices. *ACS Energy Lett.* 2016;**1**:757-763.

99. Chen P, Bai Y, Wang S, et al. In situ growth of 2D perovskite capping layer for stable and efficient perovskite solar cells. *Adv. Funct. Mater.* 2018;**28**:1706923.

100. Jiang Q, Zhao Y, Zhang X, et al. Surface passivation of perovskite film for efficient solar cells. *Nat. Photonics* 2019;**13**:460-466.

101. Feng J, Gong C, Gao H, et al. Single-crystalline layered metal-halide perovskite nanowires for ultrasensitive photodetectors. *Nature Electronics* 2018;**1**:404-410.

102. Zhu B S, He Z, Yao J S, et al. Potassium ion assisted synthesis of organic–inorganic hybrid perovskite nanobelts for stable and flexible photodetectors. *Adv. Optical Mater.* 2018;**6**:1701029.

103. Mullin J W. *Crystallization*, Elsevier, **2001**.

104. Liu Y, Ye H, Zhang Y, et al. Surface-tension-controlled crystallization for high-quality 2D perovskite single crystals for ultrahigh photodetection. *Matter.* 2019;**1**:465-480.

105. Dohner E R, Hoke E T.Karunadasa H I. Self-assembly of broadband white-light emitters. *J. Am. Chem. Soc.* 2014;**136**:1718-1721.

106. Dohner E R, Jaffe A, Bradshaw L R, et al. Intrinsic white-light emission from layered hybrid perovskites. *J. Am. Chem. Soc.* 2014;**136**:13154-13157.

107. Tyagi P, Arveson S M.Tisdale W A. Colloidal organohalide perovskite nanoplatelets exhibiting quantum confinement. *J. Phys. Chem.* 2015;**6**:1911-1916.

108. Byun J, Cho H, Wolf C, et al. Perovskite light-emitting diodes: efficient visible quasi-2D perovskite light-emitting diodes. *Adv. Mater.* 2016;**28**:7550-7550.

109. Yuan M, Quan L N, Comin R, et al. Perovskite energy funnels for efficient light-emitting diodes. *Nat. Nanotechnol.* 2016;**11**:872-877.

110. Wang N, Cheng L, Ge R, et al. Perovskite light-emitting diodes based on solution-processed self-organized multiple quantum wells. *Nat. Photonics* 2016;**10**:699-704.

111. Yuan S, Wang Z K, Xiao L X, et al. Optimization of low-dimensional components of quasi-2D perovskite films for deep-blue light-emitting diodes, *Adv. Mater.* 2019; **31**: 1904319.

112. Zhao B, Bai S, Kim V, et al. High-efficiency perovskite–polymer bulk heterostructure light-emitting diodes. *Nat. Photonics* 2018;**12**:783-789.

113. Li M, Gao Q, Liu P, et al. Amplified spontaneous emission based on 2D Ruddlesden–Popper perovskites. *Adv. Funct. Mater.* 2018;**28**:1707006.

114. Zhang H, Liao Q, Wu Y, et al. 2D Ruddlesden–Popper perovskites microring laser array. *Adv. Mater.* 2018;**30**:1706186.

115. Liu Y, Ono L K.Qi Y. Organic additive engineering toward efficient perovskite light-emitting diodes. *InfoMat.* 2020.

116. Soe C M M, Stoumpos C C, Kepenekian M, et al. New type of 2D perovskites with alternating cations in the interlayer space,$(C(NH_2)_3)(CH_3NH_3)_nPb_nI_{3n+1}$: Structure, properties, and photovoltaic performance. *J. Am. Chem. Soc.* 2017;**139**:16297-16309.

117. Mao L, Ke W, Pedesseau L, et al. Hybrid Dion–Jacobson 2D lead iodide perovskites. *J. Am. Chem. Soc.* 2018;**140**:3775-3783.

118. Ma C, Shen D, Ng T W, et al. 2D Perovskites with short interlayer distance for high-performance solar cell application. *Adv. Mater.* 2018;**30**:1800710.

119. Zhang Y, Wang P, Tang M-C, et al. Dynamical transformation of two-dimensional perovskites with alternating cations in the interlayer space for high-performance photovoltaics. *J. Am. Chem. Soc.* 2019;**141**:2684-2694.

120. Luo T, Zhang Y, Xu Z, et al. Compositional control in 2D perovskites with alternating cations in the interlayer space for photovoltaics with efficiency over 18%. *Adv. Mater.* 2019;**31**:1903848.

121. Wang H, Chan C C, Chu M, et al. Interlayer cross-linked 2D perovskite solar cell with uniform phase distribution and increased exciton coupling. *Solar RRL* 2020;**4**:1900578.

122. Xie Y, Yu H, Duan J, et al. Enhancing device performance in quasi-2D perovskite $((BA)_2(MA)_3Pb_4I_{13})$ solar cells using $PbCl_2$ additives. *ACS Appl. Mater. Interfaces* 2020;**12**:11190-11196.

123. Li X, Wu G, Zhou J, et al. Non-preheating processed quasi-2D pPerovskites for efficient and stable solar cells. *Small* 2020;**16**:1906997.

124. Lai H, Lu D, Xu Z, et al. Organic-salt-assisted crystal growth and orientation of quasi-2D Ruddlesden-Popper perovskites for solar cells with efficiency over 19%. *Adv. Mater.* 2020;**32**:2001470.

125. Yao K, Wang X, Li F, et al. Mixed perovskite based on methyl-ammonium and polymeric-ammonium for stable and reproducible solar cells. *Chem. Commun.* 2015;**51**:15430-15433.

126. Wang Z, Lin Q, Chmiel F P, et al. Efficient ambient-air-stable solar cells with 2D–3D heterostructured butylammonium-caesium-formamidinium lead halide perovskites. *Nat. Energy.* 2017;**2**:17135.

127. Grancini G, Roldán-Carmona C, Zimmermann I, et al. One-Year stable perovskite solar cells by 2D/3D interface engineering. *Nat. Commun.* 2017;**8**:1-8.

128. Herckens R, Van Gompel W T, Song W, et al. Multi-layered hybrid perovskites templated with carbazole derivatives: optical properties, enhanced moisture stability and solar cell characteristics. *J. Mater. Chem. A* 2018;**6**:22899-22908.

129. Chen J, Lee D, Park N-G J A a m, et al. Stabilizing the Ag electrode and reducing J–V hysteresis through suppression of iodide migration in perovskite solar cells. 2017;**9**:36338-36349.

130. Liu G, Xu X-X, Xu S, et al. Passivation effect of halogenated benzylammonium as a second spacer cation for improved photovoltaic performance of quasi-2D perovskite solar cells. *J. Mater. Chem. A* 2020;**8**:5900-5906.

131. Chen X, Ding M, Luo T, et al. Self-assembly of 2D/3D perovskites by crystal engineering for efficient air-processed, air-stable inverted planar perovskite solar Cells. *ACS Appl. Energy Mater.* 2020;**3**:2975-2982.

132. Li J, Wu M, Yang G, et al. Bottom-up passivation effects by using 3D/2D mix structure for high performance pin perovskite solar cells. *Solar Energy* 2020;**205**:44-50.

133. Ma C, Leng C, Ji Y, et al. 2D/3D perovskite hybrids as moisture-tolerant and efficient light absorbers for solar cells. *Nanoscale* 2016;**8**:18309-18314.

134. Cho K T, Zhang Y, Orlandi S, et al. Water-repellent low-dimensional fluorous perovskite as interfacial coating for 20% efficient solar cells. *Nano Lett.* 2018;**18**:5467-5474.

135. Chen J, Seo J Y.Park N G Simultaneous improvement of photovoltaic performance and stability by in situ formation of 2D perovskite at $(FAPbI_3)_{0.88}(CsPbBr_3)_{0.12}$/CuSCN interface. *Adv. Energy Mater.* 2018;**8**:1702714.

136. Cho K T, Grancini G, Lee Y, et al. Selective growth of layered perovskites for stable and efficient photovoltaics. *Energy Environ. Sci.* 2018;**11**:952-959.

137. Zhou Q, Liang L, Hu J, et al. High-performance perovskite solar cells with enhanced environmental stability based on a $(p-FC_6H_4C_2H_4NH_3)_2[PbI_4]$ capping layer. *Adv. Energy Mater.* 2019;**9**:1802595.

138. Min H, Kim M, Lee S-U, et al. Efficient, stable solar cells by using inherent bandgap of α-phase formamidinium lead iodide. *Science* 2019;**366**:749-753.

139. Wang X, Wang Y, Zhang T, et al. Steric mixed-cation 2D perovskite as a methylammonium locker to stabilize $MAPbI_3$. *Angew. Chem.* 2020;**132**:1485-1489.

140. Hu J, Wang C, Qiu S, et al. Spontaneously self-assembly of a 2D/3D heterostructure enhances the efficiency and stability in printed perovskite solar cells. *Adv. Energy Mater.* 2020;**10**:2000173.

141. Yangi L, Li Y, Pei Y, et al. A novel 2D perovskite as surface "patches" for efficient flexible perovskite solar cells. *J. Mater. Chem. A* 2020;**8**:7808-7818.

142. Kim H, Pei M, Lee Y, et al. Self-crystallized multifunctional 2D perovskite for efficient and stable perovskite solar cells. A*dv. Funct. Mater.* 2020;**30**:1910620.

143. Tan Z, Wu Y, Hong H, et al. Two-dimensional $(C_4H_9NH_3)_2PbBr_4$ perovskite crystals for high-performance photodetector. *J. Am. Chem. Soc.* 2016;**138**:16612-16615.

144. Pan Y, Wang H, Li X, et al. Detection range extended 2D Ruddlesden–Popper perovskite photodetectors. *J. Mater. Chem. C* 2020;**8**:3359-3366.

145. Zhao Y, Qiu Y, Gao H, et al. Layered-perovskite nanowires with long-range orientational order for ultrasensitive photodetectors. *Adv. Mater.* 2020;**32**:1905298.

146. Loi H L, Cao J, Guo X, et al. Gradient 2D/3D perovskite films prepared by hot-casting for sensitive photodetectors. *Adv. Sci.* 2020;2000776.

147. Wang Y, Tang Y, Jiang J, et al. Mixed-dimensional self-assembly organic–inorganic perovskite microcrystals for stable and efficient photodetectors. *J. Mater. Chem. C* 2020;**8**:5399-5408.

148. Liang D, Peng Y, Fu Y, et al. Color-pure violet-light-emitting diodes based on layered lead halide perovskite nanoplates. *ACS Nano* 2016;**10**:6897-6904.

149. Quan L N, Zhao Y, García de Arquer F P, et al. Tailoring the energy landscape in quasi-2D halide perovskites enables efficient green-light emission. *Nano Lett.* 2017;**17**:3701-3709.

150. Yang X, Zhang X, Deng J, et al. Efficient green light-emitting diodes based on quasi-two-dimensional composition and phase engineered perovskite with surface passivation. *Nat. Commun.* 2018;**9**:1-8.

151. Shang Y, Liao Y, Wei Q, et al. Highly stable hybrid perovskite light-emitting diodes based on Dion-Jacobson structure. *Sci. Adv.* 2019;**5**:eaaw8072.

152. Jin Y, Wang Z K, Yuan S, et al. Synergistic effect of dual ligands on stable blue quasi-2D perovskite light-emitting diodes. *Adv. Funct. Mater.* 2020;**30**:1908339.

153. Qin C, Matsushima T, Potscavage W J, et al. Triplet management for efficient perovskite light-emitting diodes. *Nat. Photonics* 2020;**14**:70-75.

154. Zhang H, Wu Y, Liao Q, et al. A two-dimensional ruddlesden–popper perovskite nanowire laser array based on ultrafast light - harvesting quantum wells. *Angew. Chem.* 2018;**130**:7874-7878.

155. Li M, Wei Q, Muduli S K, et al. Enhanced exciton and photon confinement in Ruddlesden– Popper perovskite microplatelets for highly stable low - threshold polarized lasing. *Adv. Mater.* 2018;**30**:1707235.

156. Qin C, Sandanayaka A S, Zhao C, et al. Stable room-temperature continuous-wave lasing in quasi-2D perovskite films. *Nature* 2020;**585**:53-57.

157. Lei L, Seyitliyev D, Stuard S, et al. Efficient energy funneling in quasi-2D perovskites: from light emission to lasing. *Adv. Mater.* 2020;**32**:1906571.

158. Mao L, Tsai H, Nie W, et al. Role of organic counterion in lead-and tin-based two-dimensional semiconducting iodide perovskites and application in planar solar cells. *Chem. Mater.* 2016;**28**:7781-7792.

159. Papavassiliou G C, Mousdis G A, Raptopoulou C, et al. Some new luminescent compounds based on 4-methylbenzylamine and lead halides. *Zeitschrift Fur Naturforschung B* 2000;**55**:536-540.

160. Smith I C, Hoke E T, Solis-Ibarra D, et al. A layered hybrid perovskite solar-cell absorber with enhanced moisture stability. *Angew. Chem.* 2014;**126**:11414-11417.

161. Pan H, Zhao X, Gong X, et al. Atomic-scale tailoring of organic cation of layered ruddlesden–popper perovskite compounds. *J. Phys. Chem.* 2019;**10**:1813-1819.

162. Cohen B-E, Wierzbowska M.Etgar L. High efficiency quasi 2D lead bromide perovskite solar cells using various barrier molecules. *Sustain. Energy Fuels,* 2017;**1**:1935-1943.

163. Park I H, Chu L, Leng K, et al. Highly stable two‑dimensional tin (ii) iodide hybrid organic-inorganic perovskite based on stilbene derivative. *Adv. Funct. Mater.* 2019;**29**:1904810.

164. Zhu X-H, Mercier N, Riou A, et al. $(C_4H_3SCH_2NH_3)_2(CH_3NH_3)Pb_2I_7$: non-centrosymmetrical crystal structure of a bilayer hybrid perovskite. *Chem. Commun.* 2002;2160-2161.

165. Wang Z-X, Liao W-Q, Ye H-Y, et al. Sequential structural transitions with distinct dielectric responses in a layered perovskite organic–inorganic hybrid material:$[C_4H_9N]_2[PbBr_4]$. *Dalton Trans.* 2015;**44**:20406-20412.

166. Mao L, Wu Y, Stoumpos C C, et al. White-light emission and structural distortion in new corrugated two-dimensional lead bromide perovskites. *J. Am. Chem. Soc.* 2017;**139**:5210-5215.

Table 1. Recent advancement of solar cells based on low n quasi-2D mixed perovskite (n<5)

Active layer	Device structure	PCE (%)	Stability	Year[ref]
(Gua)(MA)$_3$Pb$_3$I$_{10}$ (n=3)	ITO/PEDOT:PSS/active layer/PCBM/Al	7.26	N/A	2017[116]
(3AMP)(MA)$_3$Pb$_4$I$_{13}$ (n=4)	FTO/PEDOT:PSS/active layer/C60/BCP/Ag	7.32	N/A	2018[117]
(PDA)(MA)$_3$Pb$_4$I$_{13}$ (n=4)	ITO/PEDOT:PSS/active layer/C60/BCP/Ag	13.0	90% of initial PCE after 1000h in dark, 85% RH	2018[118]
(F-PEA)$_2$(MA)$_4$Pb$_5$I$_{16}$ (n=5)	FTO/m-TiO$_2$/active layer/spiro-OMeTAD/Au	13.64	65% of PCE after 76 h, dark, 70 C°	2019[88]
(F-PEA)$_2$(MA)$_4$Pb$_5$I$_{16}$ (n=5)	ITO/PEDOT:PSS/active layer/PCBM/BCP/Ag	14.5	90% of initial PCE after 40 days, dark, 40%–50% RH	2019[64]
(Gua)(MA)$_3$Pb$_3$I$_{10}$ (n=3)	FTO/c-TiO$_2$/active layer/spiro-OMeTAD/Au	16.84	88% of PCE after 240 days, dark, 30%–40% RH	2019[119]
(Gua)(MA)$_3$Pb$_3$I$_{10}$ (n=3)	FTO/c-TiO$_2$/active layer/spiro-OMeTAD/Au	18.48	95% of PCE after 131 days, in dark, 40% RH	2019[120]
(BDA)MA$_3$Pb$_4$I$_{13}$ (n=4)	ITO/PEDOT:PSS/active layer/PCBM/BCP/Ag	12.81	60% of PCE after 23 days, in dark, 50%-60% RH	2020[121]
(BA)$_2$(MA)$_3$Pb$_4$I$_{13}$ (n = 4)	ITO/PEDOT:PSS/active layer/PCBM/PEI/Al	15.08	N/A	2020[122]
(BA)$_{1.6}$(MA)$_{3.4}$Pb$_4$I$_{13}$ (n = 4)	FTO/PTAA/active layer/C$_{60}$/BCP/Ag	15.44	97% of PCE after 85 days, N$_2$, in dark	2020[123]
(ThMA)$_2$(FA)$_4$Pb$_5$I$_{16}$ (n = 5)	ITO/PEDOT:PSS/active layer/PCBM/BCP/Ag	19.06	96% of PCE after 576 h, N$_2$, in dark	2020[124]

Table 2. Recent advancement of solar cells based on 3D/2D mixed perovskites

Active layer	Device structure	PCE (%)	Stability	Year[ref]
$(MAPbI_3)_{0.98}[(PEI)_2PbI_4]_{0.02}$	ITO/PEDOT:PSS/active layer/$PC_{61}BM$/LiF/Ag	15.2	84% of PCE after 14 days, dark, 50% RH	2015[125]
$(AVA_2PbI_4)_{0.03}(MAPbI_3)_{0.97}$	FTO/TiO_2(compact)/TiO_2(meso)/active layer/ZnO_2/Carbon	10.10	100% of PCE after10,000 h, 55 °C, continuous light soaking	2017[126]
$BA_{0.09}(FA_{0.83}Cs_{0.17})_{0.91}Pb(I_{0.6}Br_{0.4})_3$	FTO/SnO_2/$PC_{61}BM$/active layer/spiro-OMeTAD/Au	17.2	80% of PCE after 1000 h, air, dark	2017[127]
$CA_2MA_{39}Pb_{40}I_{121}$	ITO/SnO_2/active layer/spiro-OMeTAD/MoO_3/Ag	6.6	59% of PCE after 264 h, dark, 77% RH	2018[128]
$(DA_2PbI_4)_{0.05}(MAPbI_3)_{0.95}$	ITO/SnO_2/active layer/spiro-OMeTAD/MoO_3/Ag	19.05	80% of PCE after 60 days, dark	2019[95]
$(PEA_2PbI_4)_{0.017}(MAPbI_3)_{0.983}$	FTO/c-TiO_2/m-TiO_2/active layer/spiro-OMeTAD/Ag	19.84	96% of PCE after 100 h, dark	2019[129]
$Gua_{0.1}[Cs_{0.1}(FA_{0.83}MA_{0.17})_{0.9}]_{0.9}Pb(I_{0.83}Br_{0.17})_3$	ITO/SnO_2/active layer/spiro-OMeTAD/MoO_3/Ag	21.12	N/A	2019[97]
$(HEA_{0.9}CBA_{0.1})_2(Cs_{0.1}FA_{0.9})_8Pb_9(I_{0.95}Br_{0.05})_{28}$	FTO/c-TiO_2/m-TiO_2/active layer/spiro-OMeTAD/Au	18.75	90% of PCE after 1500 h, air, dark	2020[130]
$(HEA_{0.9}FBA_{0.1})_2(Cs_{0.1}FA_{0.9})_8Pb_9(I_{0.95}Br_{0.05})_{28}$	FTO/c-TiO_2/m-TiO_2/active layer/spiro-OMeTAD/Au	17.67	85% of PCE after 1500 h, air, dark	2020[130]
$iBA_{0.1}MA_{0.9}PbI_3$	ITO/NiOx/active layer/PCBM/ZrAcac/Ag	17.48	75% of PCE after 35 days, air, dark	2020[131]
PEABr-treated $MAPbI_3$	ITO/TAPC/PEABr/active layer/$PC_{61}BM$/Bphen/Ag	19.46	86.1% of PCE after 1300 h, N_2, dark	2020[132]

Table 3. Recent advancement of solar cells based on 3D/2D perovskites with a bilayer structure

Active layer	Device structure	PCE (%)	Stability	Year[ref]
MAPbI$_x$Cl$_{3-x}$/CAI	ITO/PEDOT:PSS/active layer/PCBM/rhodamine 101/LiF/Ag	13.86	54% of PCE after 220 h, dark, >50% RH	2016[133]
Cs$_{0.1}$FA$_{0.74}$MA$_{0.13}$PbI$_{2.48}$Br$_{0.39}$/A34	FTO/c-TiO$_2$/m-TiO$_2$/active layer/spiro-OMeTAD/Au	20.13	N/A	2018[134]
(FAPbI$_3$)$_{0.88}$(CsPbBr$_3$)$_{0.12}$/5-AVA	FTO/c-TiO$_2$/m-TiO$_2$/active layer/CuSCN/Au	16.75	98% of PCE after 63 days, dark, 10% RH	2018[135]
Cs$_{0.1}$FA$_{0.74}$MA$_{0.13}$PbI$_{2.48}$Br$_{0.39}$/PEAI	FTO/c-TiO$_2$/m-TiO$_2$/active layer/spiro-OMeTAD/Au	20.1	90% of PCE after 800 h, 50 °C, continuous light soaking	2018[136]
Cs$_{0.05}$(MA$_{0.17}$FA$_{0.83}$)$_{0.95}$Pb(I$_{0.83}$Br$_{0.17}$)$_3$/PEAI	FTO/TiO$_2$/active layer/spiro-OMeTAD/Au	18.51	90% of PCE after 1000 h, dark, 60 RH	2018[99]
Cs$_{0.05}$(MA$_{0.17}$FA$_{0.83}$)$_{0.95}$Pb(I$_{0.83}$Br$_{0.17}$)$_3$/4F-PEAI	FTO/TiO$_2$/active layer/spiro-OMeTAD/Au	20.54	99% of PCE after 36 d, dark, 10%–30% RH	2019[137]
(FAPbI$_3$)$_{0.85}$(CsPbBr$_3$)$_{0.15}$/MDACl$_2$	FTO/TiO$_2$/active layer/spiro-OMeTAD/Au	23.77	90% of PCE, over 600 h, continuous light soaking	2019[138]
PTAI-MAPbI$_3$	ITO/SnO$_2$/active layer/spiro-OMeTAD/MoO$_3$/Ag	21.16	93% of PCE, over 500 h, continuous light soaking	2020[139]
MAPbI$_3$/SBLC	ITO/PTAA/active layer/PCBM/BCP/Ag	20.14	N/A	2020[140]
Cs$_{0.05}$Rb$_{0.05}$(FA$_{0.83}$MA$_{0.17}$)$_{0.95}$Pb(I$_{0.95}$Br$_{0.05}$)$_3$/PFAI	ITO/SnO$_2$/active layer/spiro-OMeTAD/Ag	21.38	70.4% of PCE, over 1000 h, N$_2$, 85 °C	2020[141]
Cs$_{0.08}$FA$_{0.77}$MA$_{0.12}$PbI$_{2.62}$Br$_{0.35}$/BnAI	ITO/m-TiO$_2$/SnO$_2$/active layer/spiro-OMeTAD/Au	20.79	91% of PCE, over 6 months, air, 85 °C	2020[142]

Table 4. Recent advancement of photodetectors based on the low-dimensional perovskites

Active layer	Morphology	R (A/W)	D* (Jones) or dark current (A)	Year[ref]
$(BA)_2PbBr_4$	Single crystal	~2100 A/W at 470 nm	10^{-10} A at 470 nm	2016[143]
$(BA)_2PbBr_4$	Nanobelt	-	1.97×10^{-8} A at 405 nm	2017[102]
$(BA)_2(MA)_3Pb_4I_{13}$	Nanowire	~1.5×10^4 A/W at 10 Hz	~4.7×10^{15} Jones at 10 Hz	2018[101]
$(BA)_4Pb_3Br_{13}$	Single crystal	-	~1.6×10^{13} Jones at 0.4 V	2018[60]
$(PEA)_2PbBr_4$	Single crystal	139.6 A/W at -5 V	1.89×10^{15} Jones at -5 V	2019[104]
Sn-doped $(PEA)_2PbI_4$	Polycrystal	6.43 A/W at 10 V, 520 nm	6.77×10^{13} Jones at 10 V, 520 nm	2020[144]
$(ThMA)_2(MA)_2Pb_3I_{10}$	Nanowire	1.1×10^4 at 30 Hz	9.1×10^{15} Jones at 120 Hz	2020[145]
$(PEA)_2(MA)_{n-1}Pb_nI_{3n+1}$	Polycrystal	149 A/W at 598 nm	2.0×10^{12} Jones at 598 nm	2020[146]
$(PEA)_2(MA)_4Pb_5I_{16}$	Microcrystal	182.63 A/W at 15 V	2.52×10^{14} Jones at 15 V	2020[147]

Table 5. Recent advancement of LEDs based on the low-dimensional perovskites

Active layer	Wavelength (nm)	EQE (%)	CE (cd/A)	Luminance (cd/m^2)	Year[ref]
PEA$_2$PbBr$_4$	410	0.04	-	-	2016[148]
PEA$_2$(MA$_{n-1}$Pb$_n$I$_{3n+1}$)	760	8.8	-	-	2016[109]
(NMA)$_2$(MA$_{n-1}$Pb$_n$I$_{3n+1}$)	763	11.7	-	-	2016[110]
PEA$_2$(MA$_{n-1}$Pb$_n$Br$_{3n+1}$)	526	7.4	4.9	8400	2017[149]
PEA$_2$(FAPbBr$_3$)$_2$PbBr$_4$	532	14.36	62.43	9120	2018[150]
(BAB)(FA$_{n-1}$Pb$_n$I$_{3n+1}$)	776	4.2	-	-	2019[151]
PEA$_2$Cs$_2$Pb$_3$Br$_{10}$	508	-	-	-	2020[152]
NPA$_1$Cs$_2$Pb$_3$Br$_{10}$	480	0.086	0.1	8	2020[152]
PEA$_2$NPA$_1$Cs$_2$Pb$_3$Br$_{12}$	485	2.62	15	1200	2020[152]
PEABr-FAPbBr$_3$	527	12.4	52.1	5200	2020[153]
NMABr-FAPbBr$_3$	520	3.4	16.3	500	2020[153]

Table 6. Recent advancement of lasers based on the low-dimensional perovskites

Active layer	Morphology	Crystallinity	Pump source	Lifetime (Laser shots)	Year[ref]
$(BA)_2(MA)_5Pb_6Br_{19}$	Micro-ring	Polycrystal	400 nm, 150 fs, 1kHz	>3.6×10^6	2018[114]
$(BA)_2(FA)_2Pb_3Br_{10}$	Nanowire	Polycrystal	400 nm, 150 fs, 1kHz	>2.16×10^7	2018[154]
$(OA)_2(MA)_{n-1}Pb_nBr_{3n+1}$	Micro-platelet	Polycrystal	400 nm, 150 fs, 1kHz	>4×10^7	2018[155]
$(NMA)_2(FA)Pb_2Br_6$	Film	Polycrystal	400 nm, 150 fs, 1kHz	>1.2×10^8	2018[113]
PEABr-FAPbBr$_3$	Film	Polycrystal	488 nm	Unchanged after 1h, air	2020[156]
NMABr-FAPbBr$_3$	Film	Polycrystal	488 nm	Unchanged after 1h, air	2020[156]
$(PEA)_2(FA)_3Pb_4Br_{13}$	Film	Polycrystal	400 nm, 150 fs, 1kHz	-	2020[157]
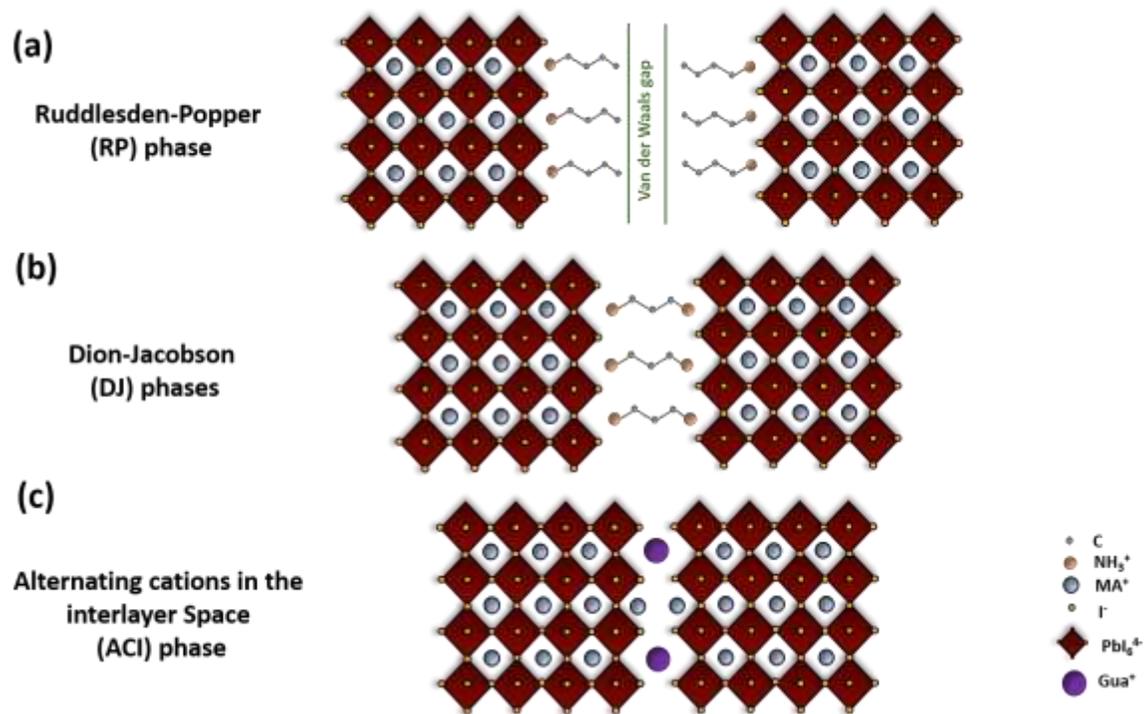
Scheme 1. Schematic of (a) Ruddlesden-Popper (RP) phase, (b) Dion-Jacobson (DJ) phase and (c) alternating cations in the interlayer space (ACI) phase 2D perovskite, where Gua is Guanidinium.
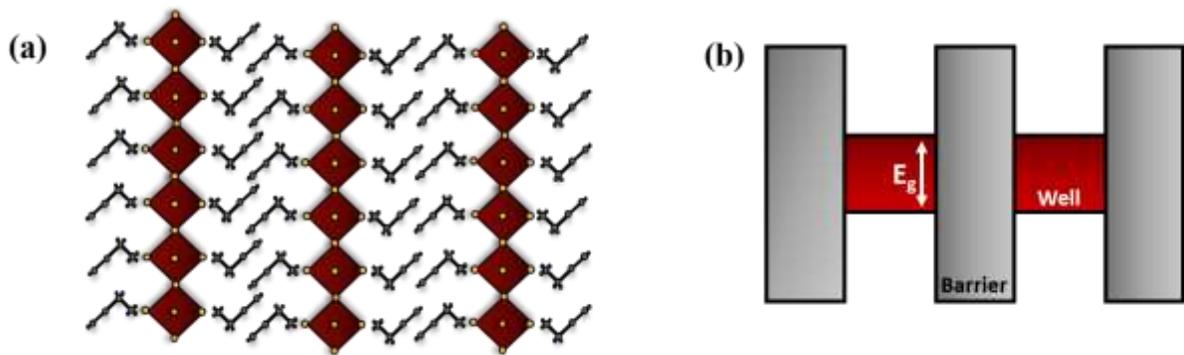
Scheme 2. (a) Schematic of multiple quantum wells structure and (b) correlated electronic band structure.
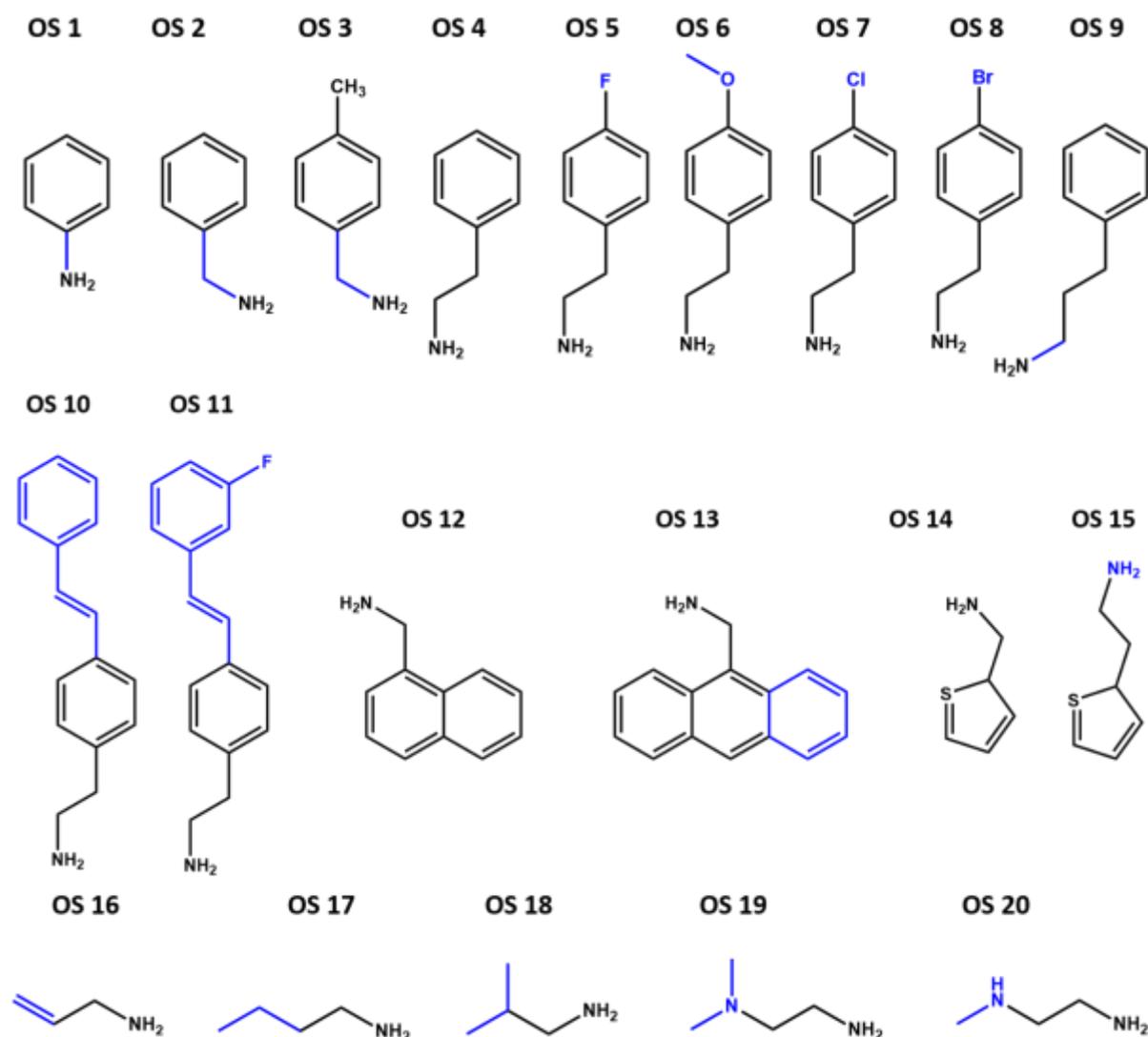
Scheme 3. Chemical structure of the organic spacer (OS) cations reported in low dimensional perovskite solar cells. OS 1: phenylammonium (PA);[63] OS 2: benzylammonium (BZA);[158] OS 3: 4-methylbenzylammonium;[159] OS 4: phenylethylammonium (PEA);[160] OS 5: 4-fluorophenylethylammonium (F-PEA);[88] OS 6: 4-methoxyphenethylammonium (MeO-PEA);[64] OS 7: 2-(4-chlorophenyl) ethanaminium (Cl-PEA);[161] OS 8: 2-(4-bromophenyl) ethanaminium (Br-PEA);[161] OS 9: propyl phenyl ammonium (PPA);[162] OS 10: 2-(4-stilbenyl)ethanammonium (SA);[163] OS 11: 2-(4-(3-fluoro)stilbenyl)ethanammonium (FSA);[163] OS 12: 1-naphthalenemethylammonium (NpMA);[89] OS 13: 9-anthracenemethylammonium (AnMA);[89] OS 14: 2-thienylmethylammonium (ThMA);[164] OS 15: 2-(2-thienyl)ethanaminium;[164] OS 16: allylammonium (ALA);[66] OS 17: n-butylammonium (n-BA+);[126] OS 18: isobutylammonium (iso-BA);[165] OS 19: 2-(dimethylamino)ethylammonium (DMEN);[166] OS 20: N1-methylpropane-1,3-diammonium (N-MPDA).[105]
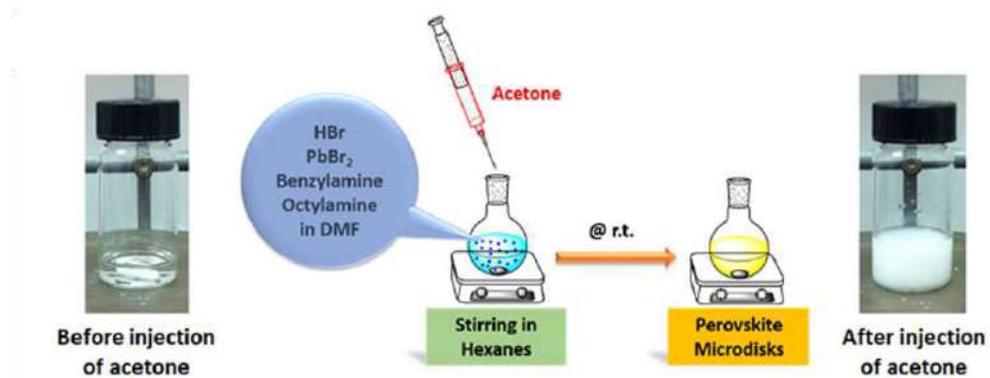
Scheme 4. Schematic synthetic steps of 2D perovskite micro-disks. Reproduced with permission from ref. 64. Copyright 2016 Royal Society of Chemistry.
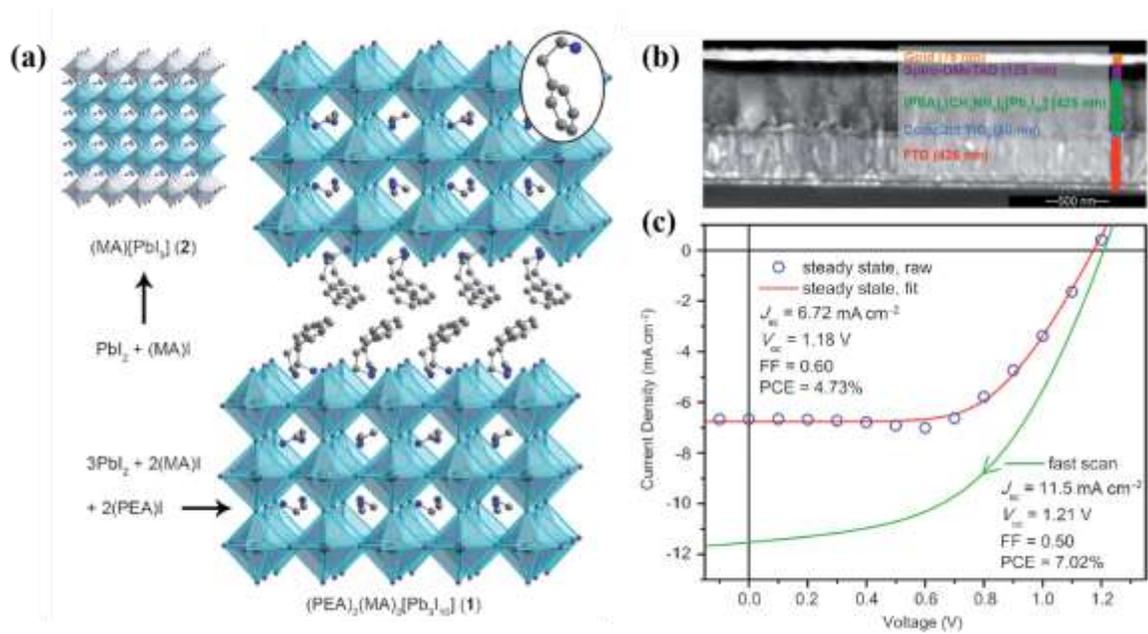
Figure 1. (a) The crystal structure of the 2D perovskite $(PEA)_2(MA)_2Pb_3I_{10}$. (b) SEM cross-section images and device configuration of planar devices. (c) The J-V curves for the devices fabricated as in (b). Reproduced with permission from ref. 44. Copyright 2014 Wiley.
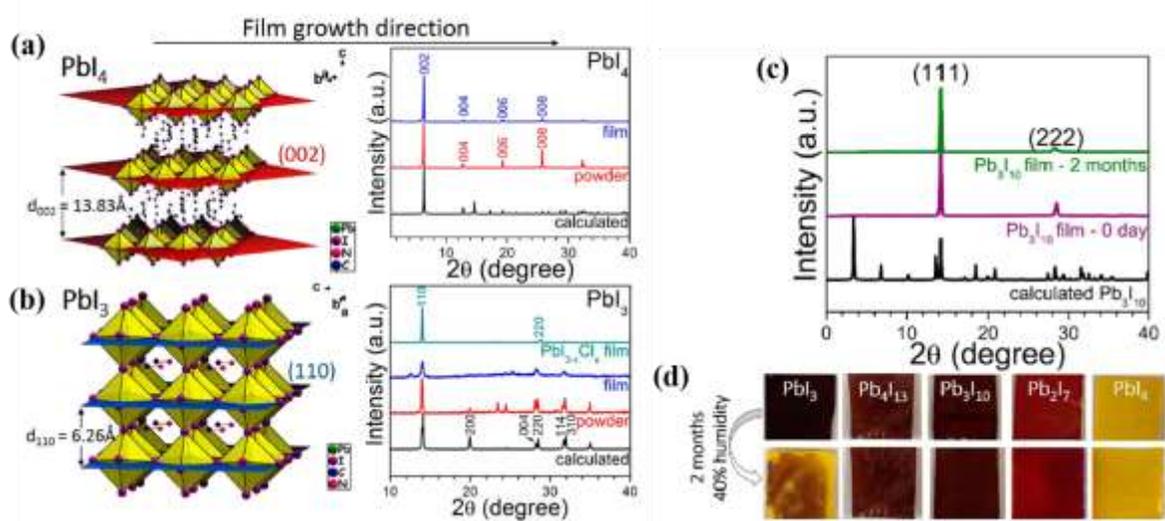
Figure 2. The XRD patterns of thin film of (a) BA_2PbI_4 and (b) $MAPbI_3$, with respective diffraction planes. (c) XRDs of fresh and aged $(BA)_2(MA)_2Pb_3I_{10}$ film. (d) Images of different perovskite films before and after exposure to humidity. Reproduced with permission from ref. 62. Copyright 2015. American Chemical Society.
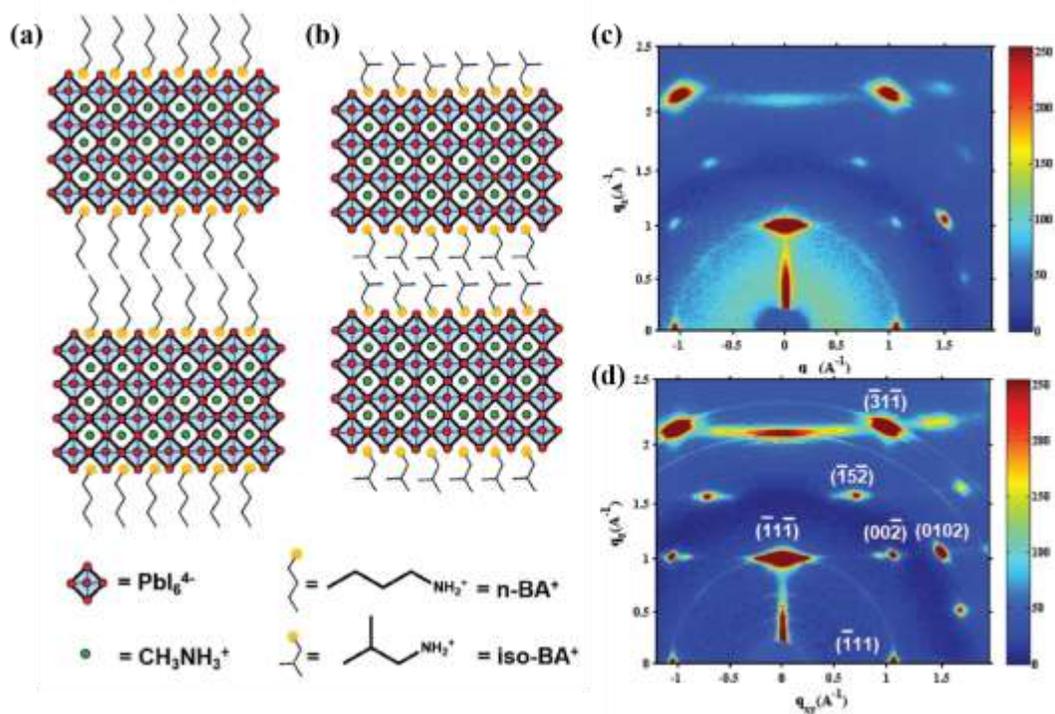
Figure 3. Schematic crystal structure of (a) $(n\text{-BA})_2(MA)_3Pb_4I_{13}$ and (b) $(n\text{-BA})_2(MA)_3Pb_4I_{13}$. The GIWAXS images of $(n\text{-BA})_2(MA)_3Pb_4I_{13}$ perovskite processed under (c) room temperature and (d) hot casting method. Reproduced with permission from ref. 76. Copyright 2017. Wiley.
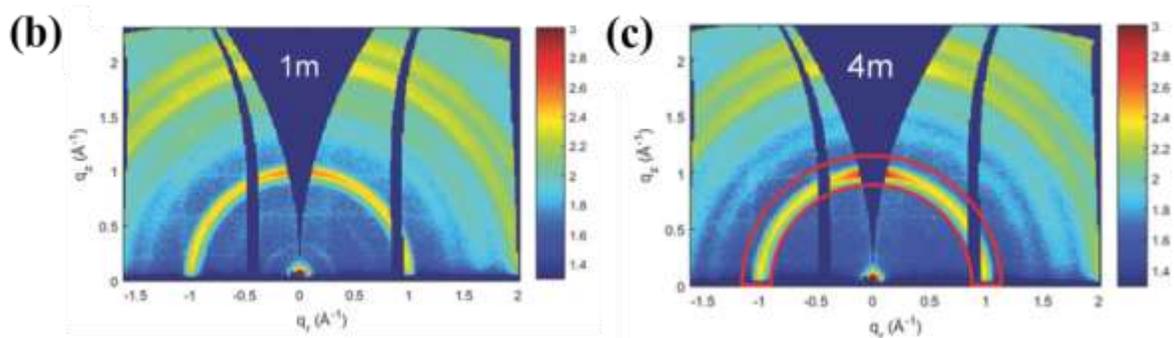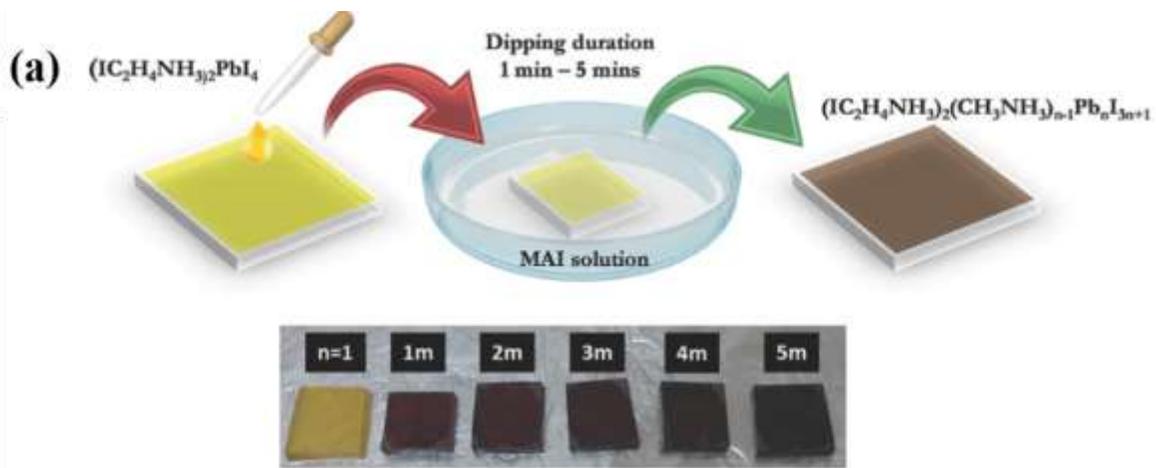
Figure 4. (a) Schematic illustration of fabrication of $(IC_2H_4NH_3)_2(CH_3NH_3)_{n-1}Pb_nI_{3n+1}$ perovskite. 2D GIWAXS data of (b) 1 minute dipping time and (c) 5 minutes dipping time. Reproduced with permission from ref. 77. Copyright 2016. Wiley.
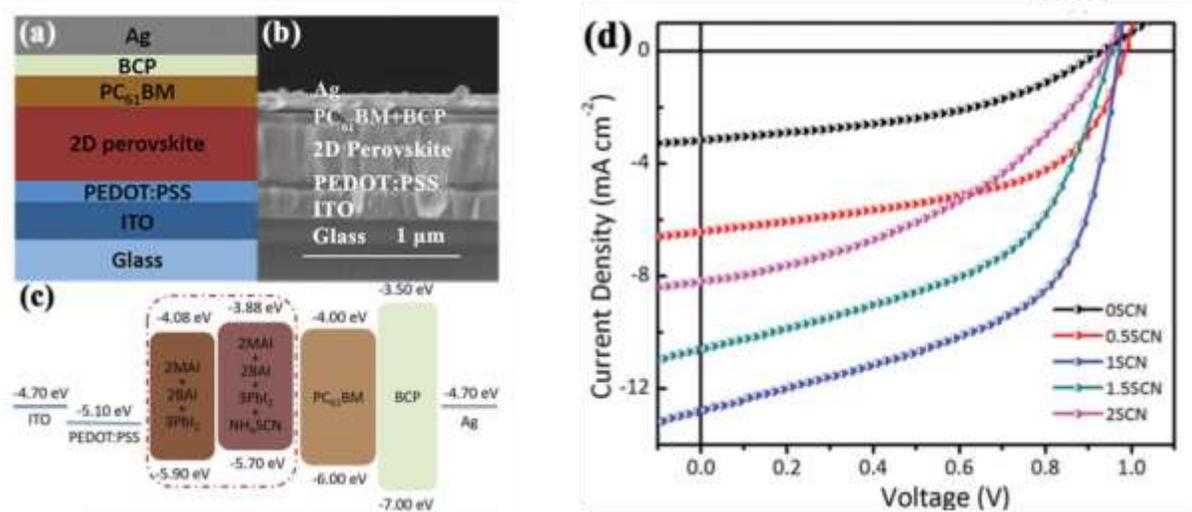
Figure 5. (a) Planar structured PSCs device configuration, (b) the cross sectional SEM image of the device applying thermal annealed $(BA)_2(MA)_2Pb_3I_{10}$-based perovskite film (1SCN) as active layer, (c) energy band alignment, and (d) the J–V curves of $(BA)_2(MA)_2Pb_3I_{10}$ based perovskite solar cells with various amounts of NH_4SCN additive under 1 sun condition (100 mW cm^{-2}). Reproduced with permission from ref. 81. Copyright 2017. Wiley.
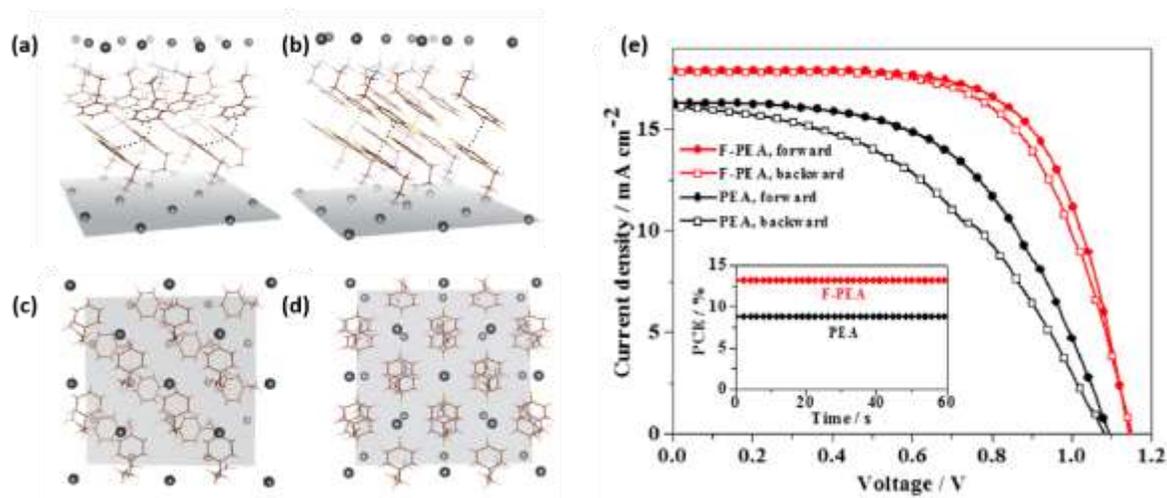
Figure 6. The structures of (a, c) $(PEA)_2PbI_4$ and (b, d) $(F\text{-}PEA)_2PbI_4$ based single-crystal XRD. (e) J-V curves of PSCs based on n = 5 2D $(PEA)_2MA_4Pb_5I_{16}$ and $(F\text{-}PEA)_2MA_4Pb_5I_{16}$ films with a bias step of 10 mV. Inset shows the stabilized power output of the corresponding devices. Reproduced with permission from ref. 88. Copyright 2019. American Chemical Society.
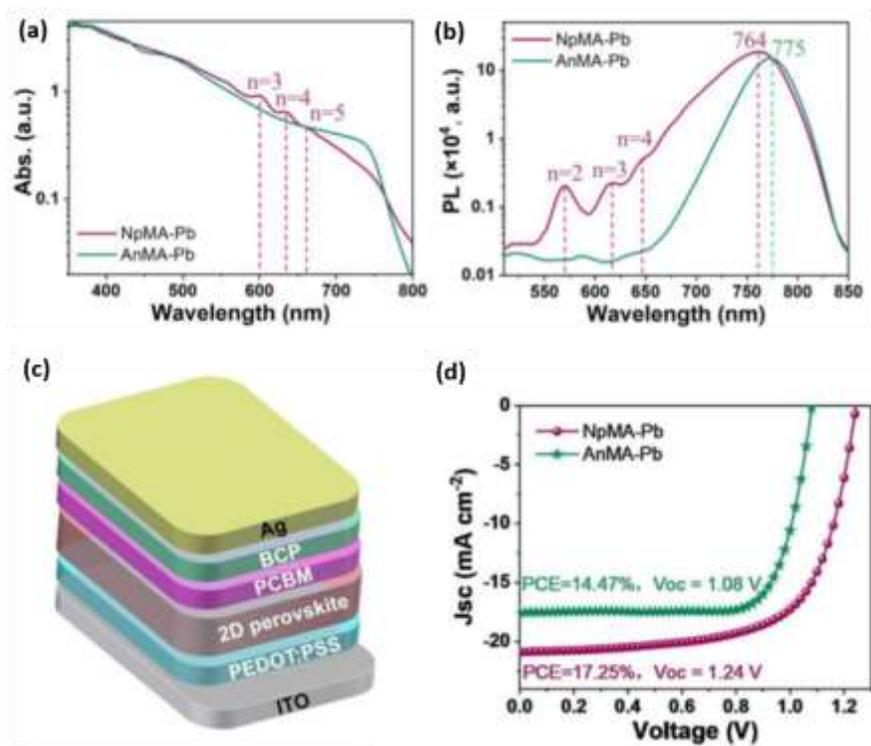
Figure 7. (a) The absorption and (b) PL spectra of the NpMA and AnMA films. (c) Device structure of NpMA and AnMA-based PSCs. (d) The J-V curves of the 2D PSCs. Reproduced with permission from ref. 89. Copyright 2020. American Chemical Society.
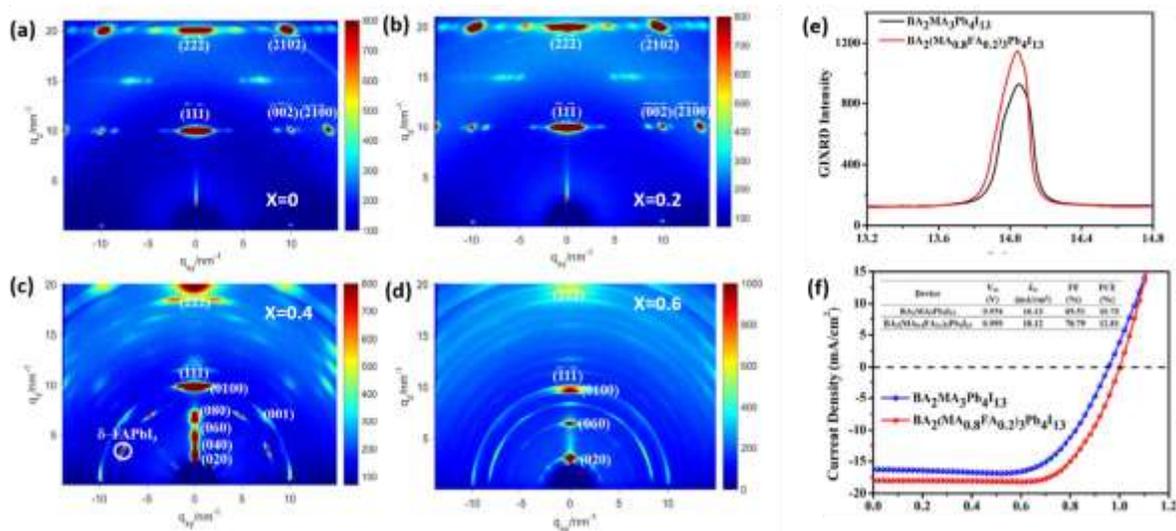
Figure 8. GIWAXS patterns of the perovskite films of $(BA)_2(MA_{1-x}FA_x)_3Pb_4I_{13}$ x= (a) 0, (b) 0.2, (c) 0.4, (d) 0.6 films, respectively. (e) GIXRD patterns of $BA_2(MA)_3Pb_4I_{13}$ and $(BA)_2(MA_{0.8}FA_{0.2})_3Pb_4I_{13}$ thin films. (f) The best J-V curve of $BA_2(MA)_3Pb_4I_{13}$ and $(BA)_2(MA_{0.8}FA_{0.2})_3Pb_4I_{13}$ based perovskite solar cells by adopting invert device structure. Reproduced with permission from ref. 90. Copyright 2018. American Chemical Society.
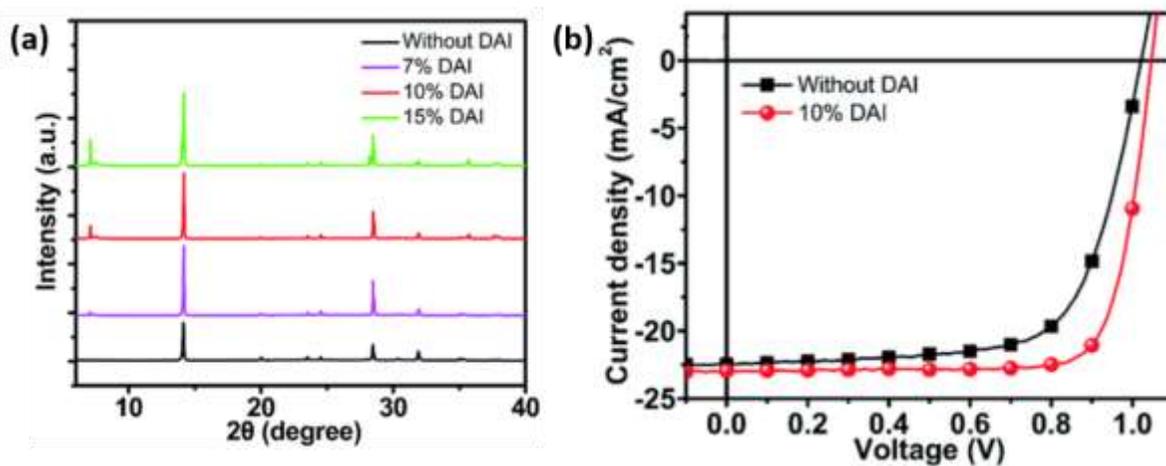
Figure 9. (a)The XRD patterns of perovskite without and with 7%, 10% and 15% DAI contents. (b) The J-V characteristics of the perovskite devices without and with 10% DAI contents. Reproduced with permission from ref. 95. Copyright 2019. Royal Society of Chemistry.
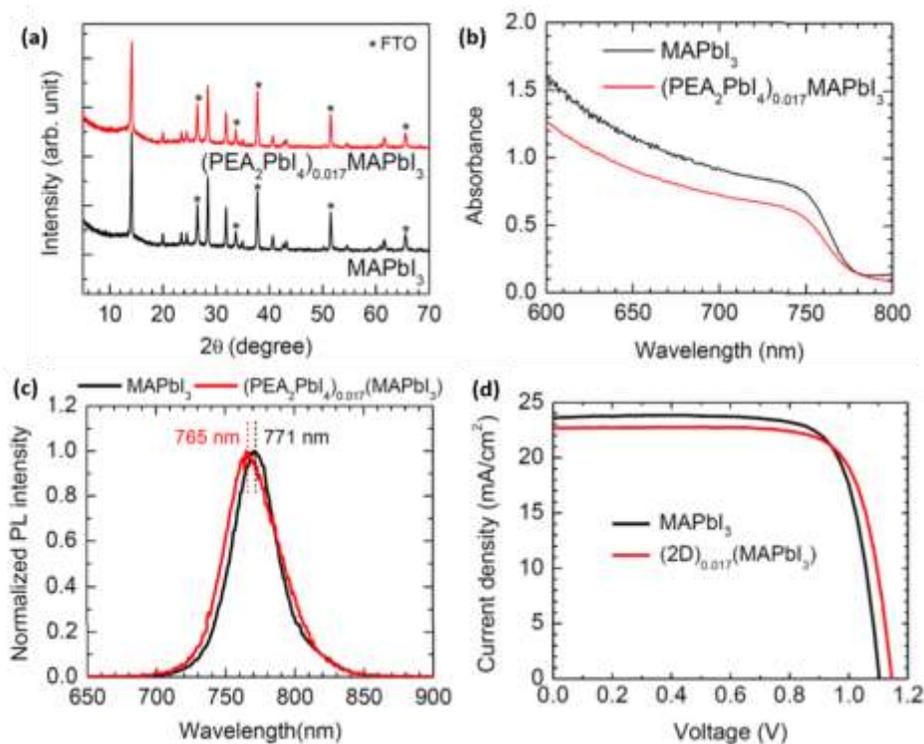
Figure 10. The XRD patterns of $MAPbI_3$ and $(PEA_2PbI_4)_{0.017}(MAPbI_3)$ films spin-coated on FTO-coated glass substrate. (b) UV−visible absorption and (c) the steady-state PL spectra of $MAPbI_3$ and $(PEA_2PbI_4)_{0.017}(MAPbI_3)$ films spin-coated on glass. (d) The J−V curves of the best-performing devices employing $MAPbI_3$ and $(PEA_2PbI_4)_{0.017}(MAPbI_3)$. Reproduced with permission from ref. 96. Copyright 2017. American Chemical Society.
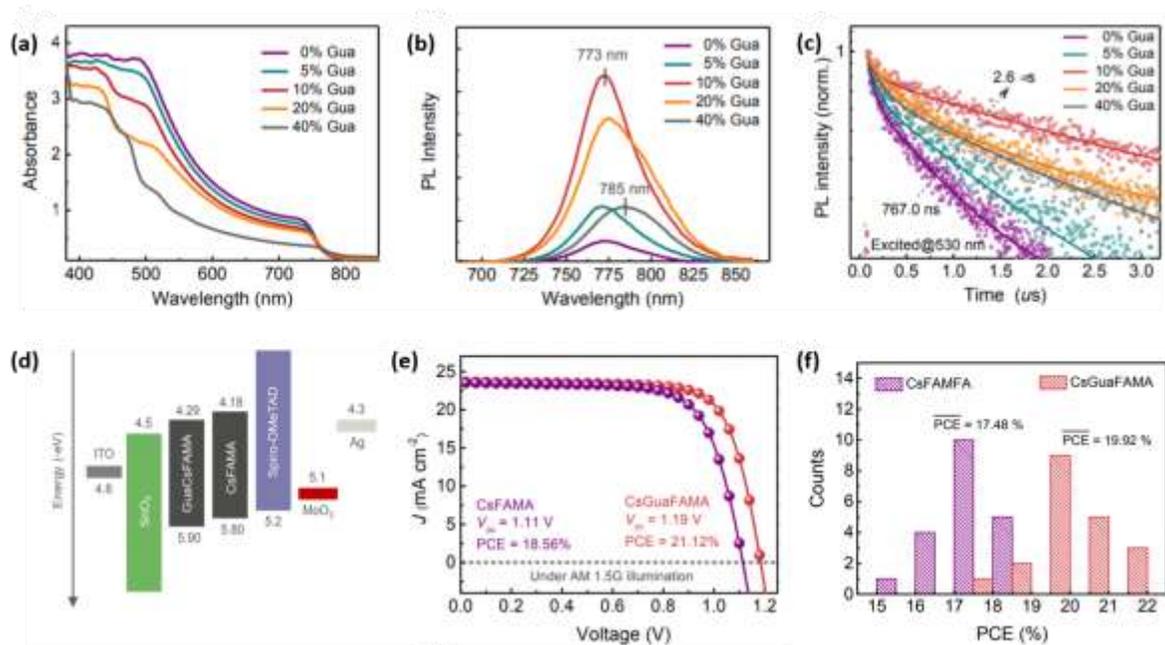
Figure 11. (a) UV-vis spectra, (b) photoluminescence and (c) the time-resolved photoluminescence (TRPL) spectra of the solid perovskite films with different Gua/CsFAMA ratio. (d) Energy level diagrams for different materials. (e) The J-V curves. (f) The PCE distribution of PSCs. Reproduced with permission from ref. 97. Copyright 2019. Royal Society of Chemistry.
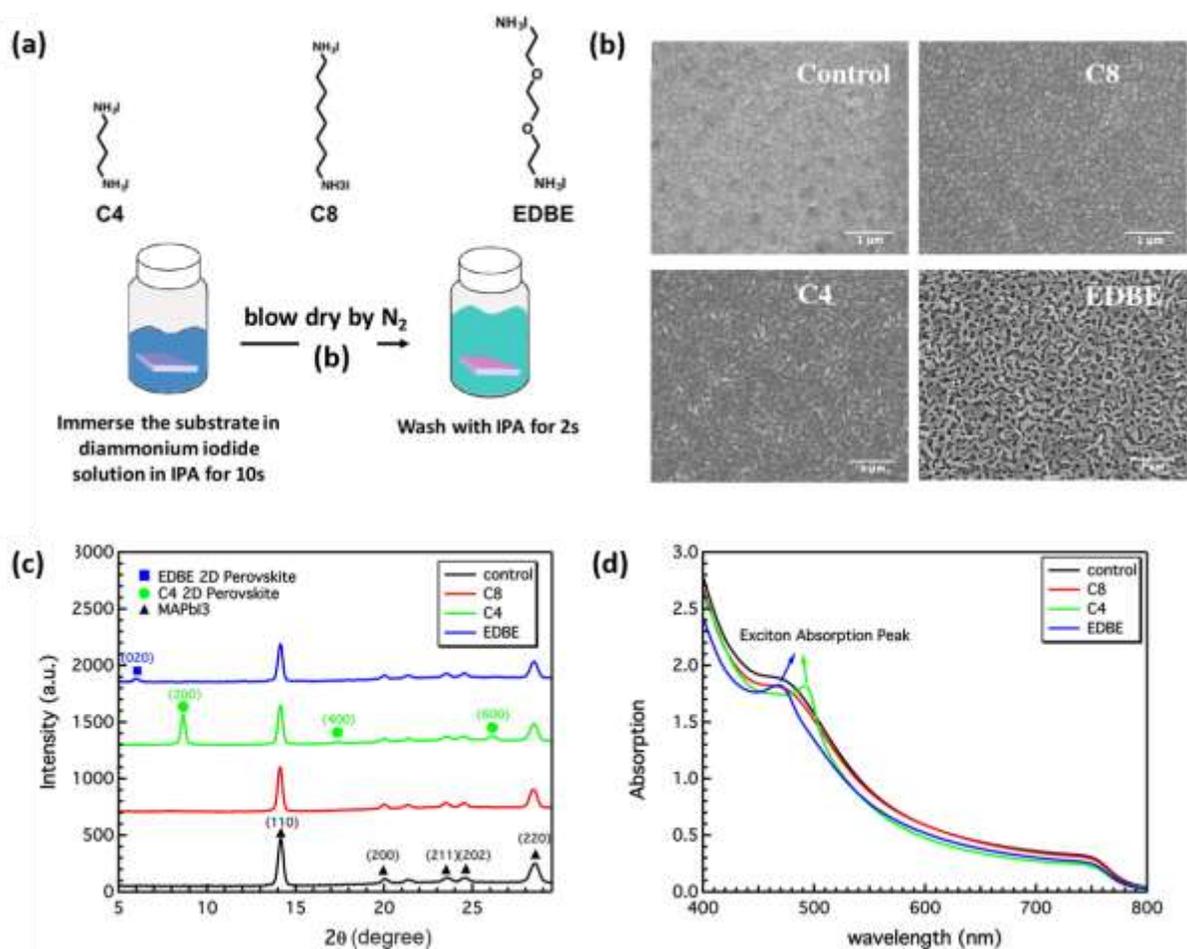
Figure 12. (a) Three kinds of diammonium iodide salts (abbreviated C4, C8, and EDBE) selected for perovskite passivation and the processing details. (b) The SEM images where the scale bar corresponds to 1 μm. (c) XRD and (d) UV-absorption of control film (MAPbI₃) and C8-, C4-, and EDBE-treated films. Reproduced with permission from ref. 98. Copyright 2016. American Chemical Society.
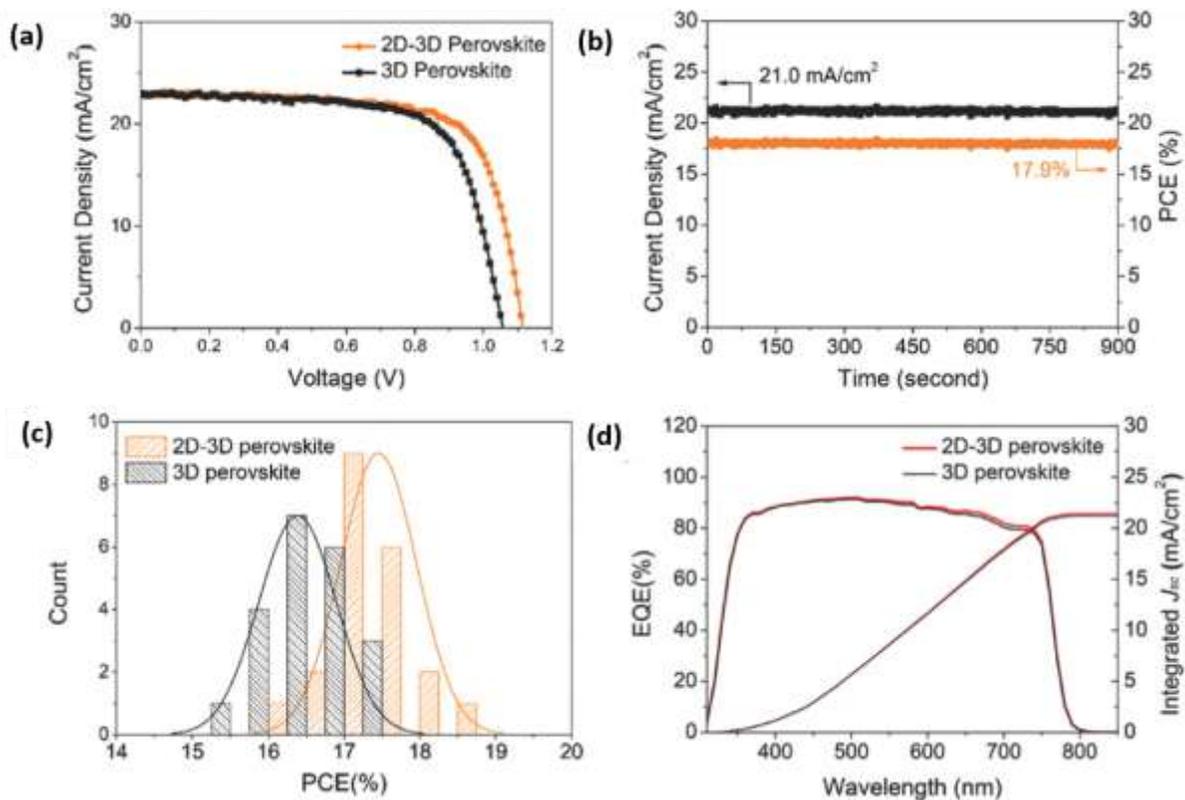
Figure 13. (a) The J–V curves of the best fabricated 3D PSCs and 2D‑3D PSCs under reverse scans, (b) The stabilized photocurrent measurement at the maximum power point (0.85 V) of 2D‑3D PSCs, (c) The statistics of the PCE distribution of the fabricated 3D PSCs (21 devices) and 2D‑3D PSCs (21 devices) under reverse scans, and (d)The IPCE measurement and the integrated J_{SC} of the fabricated 3D PSCs and 2D‑3D PSCs. Reproduced with permission from ref. 99. Copyright 2018. Wiley.
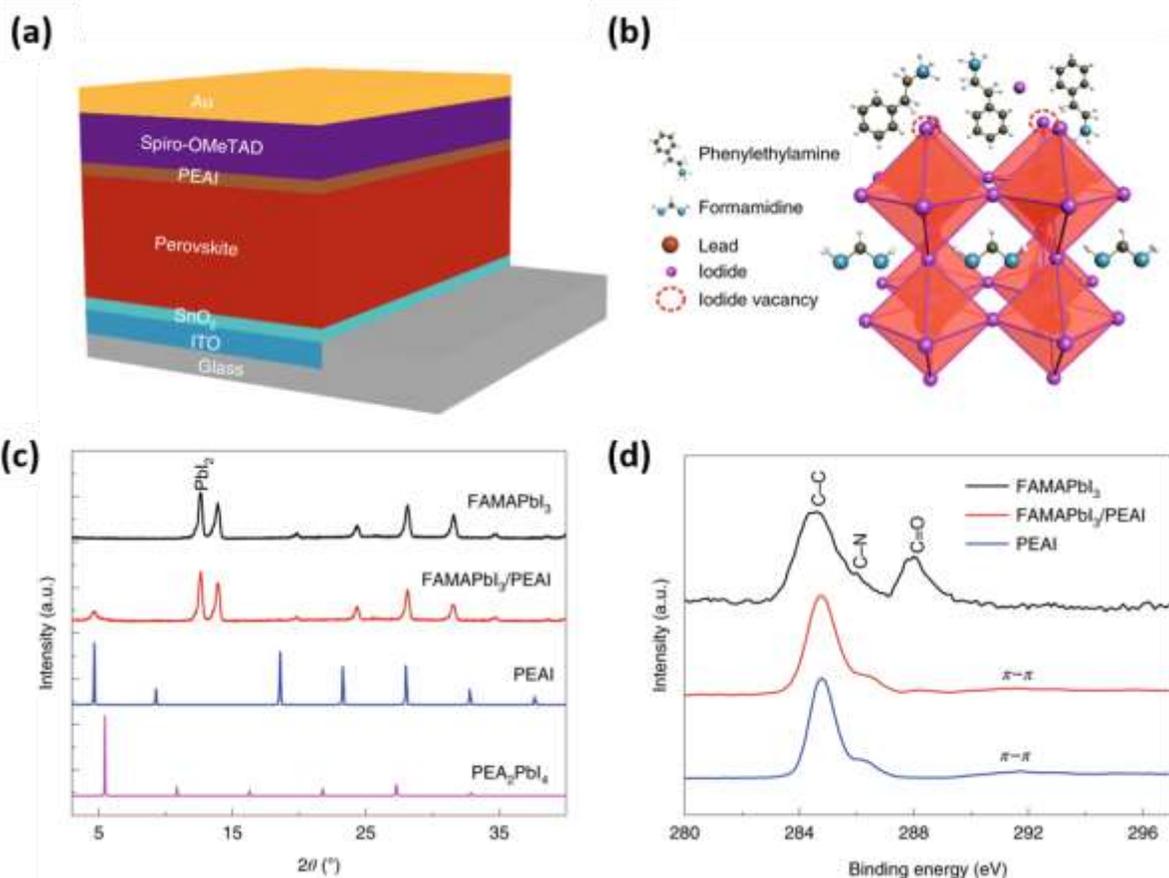
Figure 14. (a) The device structure adopted in this study. PEAI is used for post-treatment of the perovskite surface. (b) Possible passivation mechanism of the PEAI layer for the perovskite film. (c) GIXRD patterns of perovskite films before and after PEAI treatment. The diffraction patterns of the PEAI powder and of the PEA_2PbI_4 film are also shown. (d) The XPS spectra of the perovskite before and after PEAI treatment, and of the pure PEAI film. The C 1s core-level energy spectra are shown for comparison. Reproduced with permission from ref. 100. Copyright 2019. Nature Publishing Group.
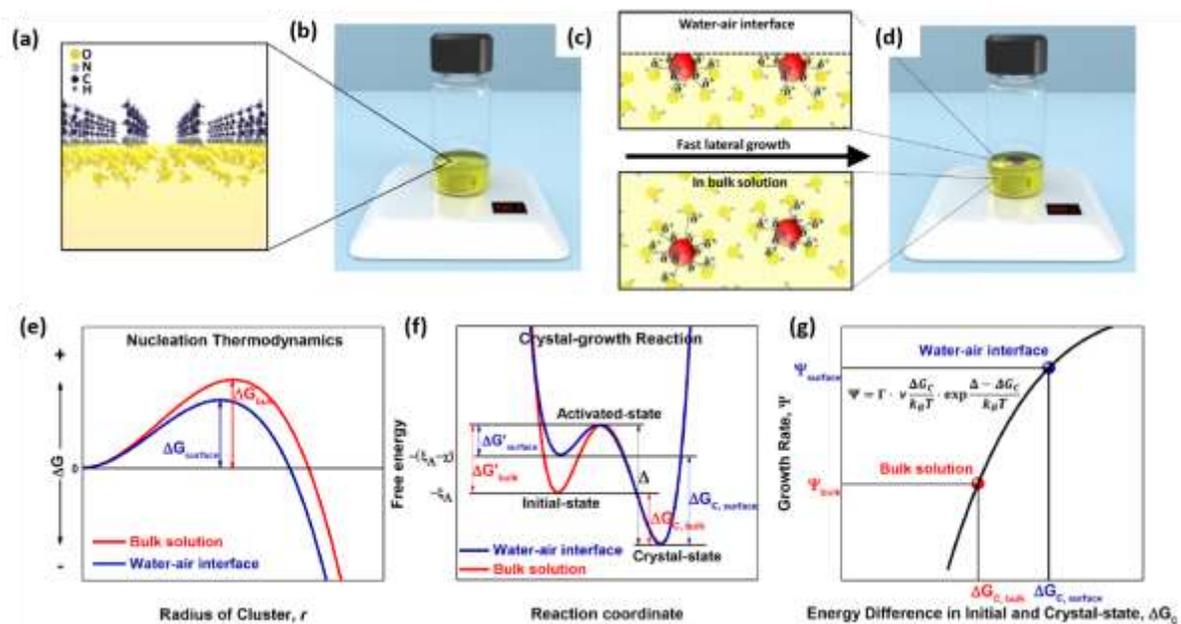
Figure 15. Crystallization of quasi-2D perovskite SCMs. (a) Schematic illustration of the alignment of butylammonium cation surfactant at the water-air interface for templating the nucleation. (b) Experimental setup during nucleation. (c) Molecular interaction between precursor molecule (red) and water molecules (yellow). Lower interaction energy is expected for the surface layer molecules due to the surface tension effect compared to those in bulk solution. (d) Experimental setup during crystal growth. Graphic illustrations on (e) the lower nucleation barrier, (f) the larger free energy changes during crystal growth, and (g) the higher growth rate of the precursor molecules at the water-air interface compared to those in bulk solution.1%). Reproduced with permission from ref. 60. Copyright 2018. American Chemical Society.
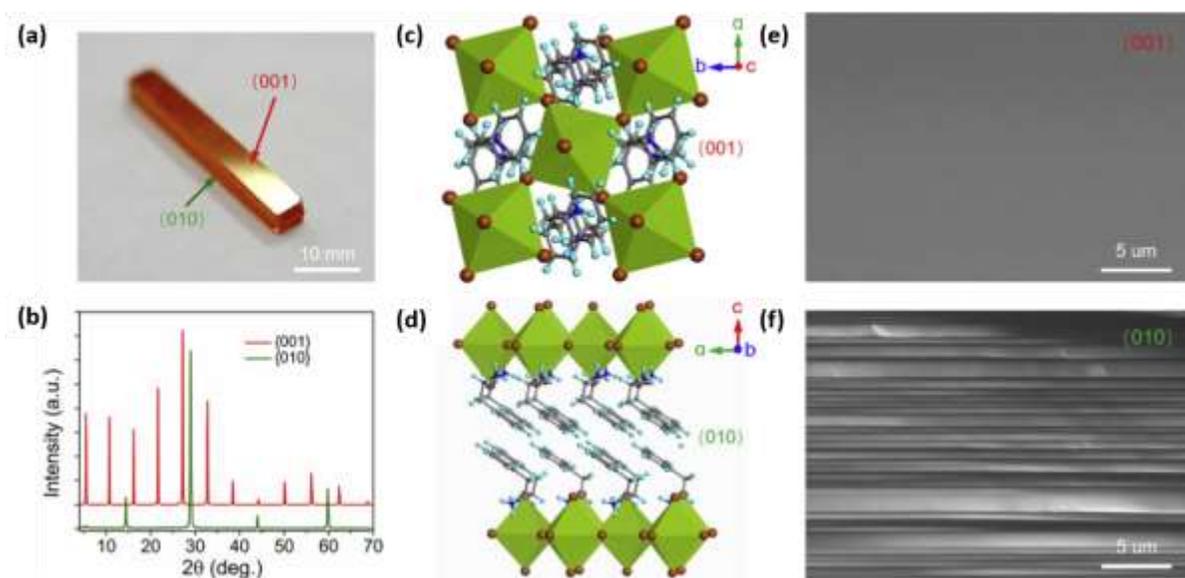
Figure 16. (a) Photograph of a well-shaped $36 \times 6 \times 6$-mm^3 bulk 2D (PEA)$_2$PbI$_4$ PSC. (b) XRD patterns of a 2D (PEA)$_2$PbI$_4$ PSC recorded from (001) and (010) planes. (c and d) Optimized crystal structures on (001) (c) and (010) (d) facets of (PEA)$_2$PbI$_4$. SEM image of (PEA)$_2$PbI$_4$ PSC for the (001) (e) and (010) (f). Reproduced with permission from ref. 104. Copyright 2019. Elsevier.
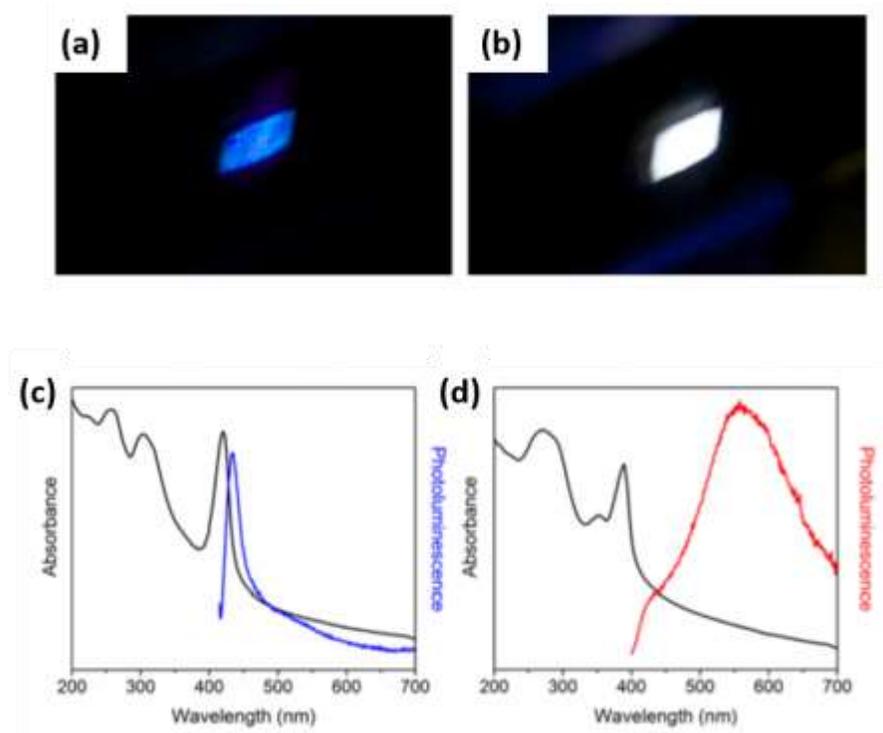
**Figure 17.** Photographs showing luminescence from powders of (a) (N-MPDA)[PbBr$_4$] and (b) (N-MEDA)[PbBr$_4$] under 380 nm irradiation. Photographs showing luminescence from powders of (c) (N-MPDA)[PbBr$_4$] and (d) (N-MEDA)[PbBr$_4$] under 380 nm irradiation. Reproduced with permission from ref. 105. Copyright 2014. American Chemical Society.
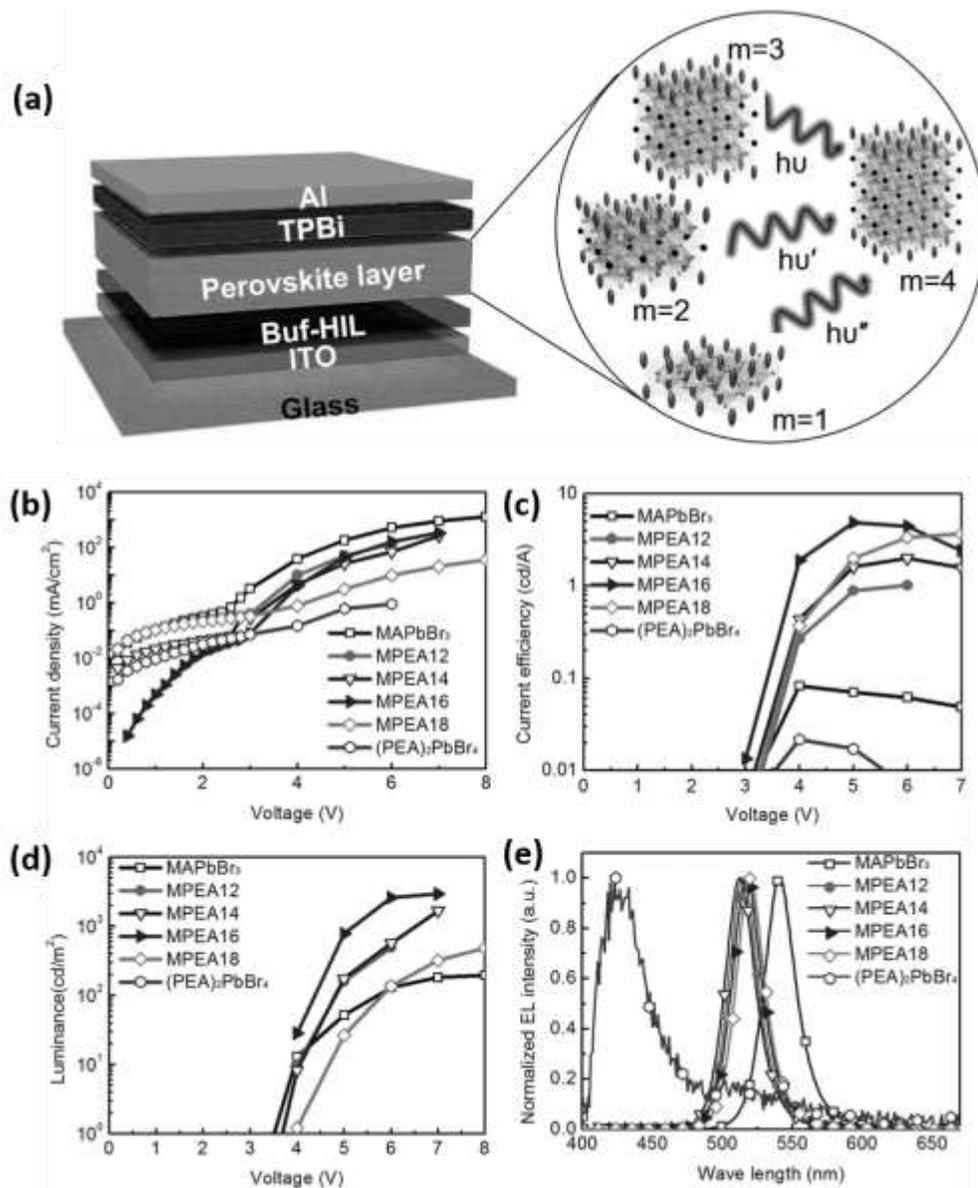
Figure 18. (a) Schematic diagram of the quasi-2D PeLEDs structurePerformance of quasi-2D PeLEDs with ITO/Buf-HIL (50 nm)/perovskite film/TPBI (50 nm)/LiF (1 nm)/Al (100 nm) structure. (b) current density versus voltage (c) current efficiency versus voltage (d) luminance versus voltage (e) The normalized EL spectra. Reproduced with permission from ref. 108. Copyright 2016, Wiley.
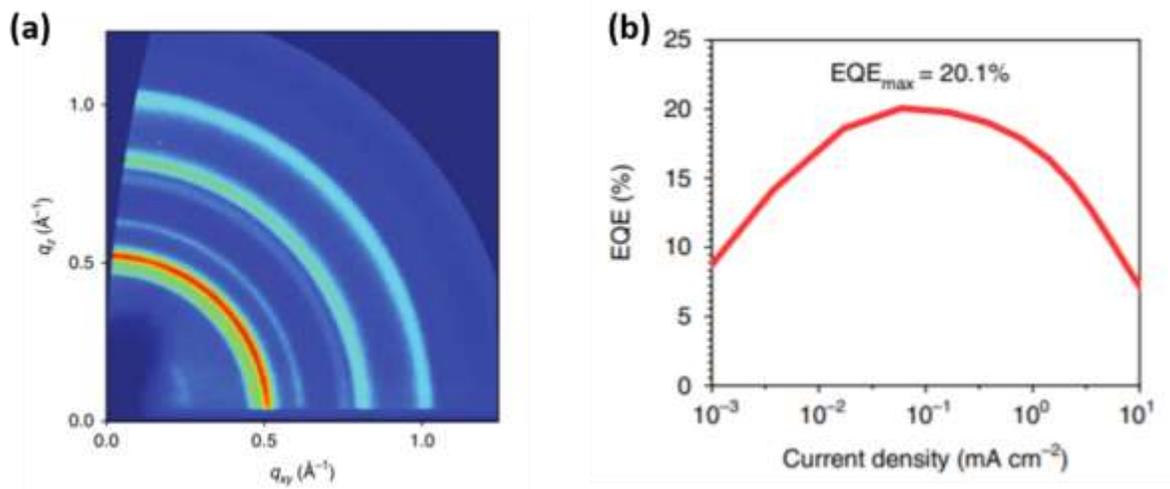
Figure 19. (a) The GIWAXS patterns of a PPBH layer deposited on silicon, (b) The EQE–current density characteristics of the best PPBH LED (peak EQE = 20.1%). Reproduced with permission from ref. 112. Copyright 2018, Nature Publishing Group.